JOURNAL OF GEOPHYSICAL RESEARCH, VOL. 114, B06401, doi:10.1029/2008JB006066, 2009



# Instantaneous dynamics of the cratonic Congo basin

Nathan J. Downey[1,2] and Michael Gurnis[1]

Received 2 September 2008; revised 16 February 2009; accepted 26 February 2009; published 3 June 2009.

[1] Understanding the formation mechanisms of cratonic basins provides an examination of the rheological, compositional and thermal properties of continental cratons. However, these mechanisms are poorly understood because there are few currently active cratonic basins. One cratonic basin thought to be active is the Congo basin located in equatorial Africa. The Congo basin is coincident with a large negative free-air gravity anomaly, an anomalous topographic depression, and a large positive upper mantle shear wave velocity anomaly. Localized admittance models show that the gravity anomaly cannot be explained by a flexural support of the topographic depression at the Congo. We analyze these data and show that they can be explained by the depression of the Congo basin by the action of a downward dynamic force on the lithosphere resulting from a high-density object within the lithosphere. We formulate instantaneous dynamic models describing the action of this force on the lithosphere. These models show that the gravity and topography of the Congo basin are explained by viscous support of an anomalously dense region located at 100 km depth within the lithosphere. The density anomaly has a magnitude within the range of 27–60 kg $m^{-3}$ and is most likely compositional in origin. Our models do not provide a constraint on the lithospheric viscosity of the Congo craton because the shallow location of the anomaly ensures strong coupling of the anomaly to the surface regardless of viscosity structure.

**Citation:** Downey, N. J., and M. Gurnis (2009), Instantaneous dynamics of the cratonic Congo basin, *J. Geophys. Res.*, *114*, B06401, doi:10.1029/2008JB006066.

## 1. Introduction

[2] Our understanding of the rheology of the lithosphere comes primarily from observations and modeling of active and ancient lithospheric deformation. On a large scale, this deformation is usually coincident with either modern or ancient plate boundaries. Interpretation of these deformation processes becomes more difficult the farther back in time they occurred, due to tectonic overprinting or erosion. Consequently, for regions where little deformation has occurred or that have not recently been associated with plate boundary processes, such as continental cratons, there are few observational constraints on lithospheric rheology.

[3] One type of cratonic deformation that has occurred throughout the geologic record is the vertical motions associated with the development of intracratonic sedimentary basins. These basins are observed in the major cratonic areas, and are often significant sources of hydrocarbons. As a result, these basins have been well studied, especially the Paleozoic Michigan, Illinois and Williston basins of North America. The relation between the forces driving intracratonic basin subsidence and the style and magnitude of that subsidence is determined by the structure, rheology and composition of cratonic lithosphere. By modeling cratonic basin subsidence it is possible to estimate the rheology of the subcratonic lithosphere and asthenosphere and to quantify the magnitude of buoyancy within cratonic lithosphere. Thus, understanding the formation mechanisms of intracratonic basins is important not only for economic reasons, but also for understanding the mechanical properties of cratonic lithosphere.

[4] Intracratonic sedimentary basins, defined in terms of their plate tectonic setting, are basins contained within continental interiors and not associated with plate boundaries [*Ingersoll and Busby*, 1995]. Despite the economic and geodynamic importance of intracratonic basins, their formation mechanisms are still not fully understood. This lack of understanding partly results from the unusual properties of these basins [*Sloss*, 1990]. The most successful formation mechanisms rely on motions of anomalous masses in the lithosphere and/or asthenosphere caused by changes in the stress state or thermal structure of the lithosphere during supercontinent breakup and/or formation [*DeRito et al.*, 1983; *Sloss*, 1990]. However, these models have not been fully explored because the relation between mantle flow and surface deformation was poorly understood when they were proposed. In addition, verification of these mantle flow models requires detailed knowledge of the dynamic subsidence and gravity fields associated with the basin-forming event. Since there are few modern active intracratonic basins these data are generally not available; the primary

[1] Seismological Laboratory, California Institute of Technology, Pasadena, California, USA.
[2] Now at Institute for Geophysics, University of Texas at Austin, Austin, Texas, USA.


0148-0227/09/2008JB006066$09.00

barrier to understanding intracratonic basin formation is the lack of modern active intracratonic basins.

[5] Intracratonic basins that are thought to be currently active are the Hudson Bay, Chad and Congo basins. The Chad basin is currently, and for much of its history since the Neogene has been, the location of a variable-sized lake at the center of an endoreic watershed (Figure 1). The sedimentary fill of the Chad basin covers an area of $8 \times 10^5$ km$^2$, is approximately 500 m thick and consists largely of lacustrine sediments deposited in a continental environment [*Burke*, 1976]. *Burke* [1976] hypothesized that deposition at the location of Lake Chad is a passive response to erosion of surrounding dynamic uplifts.

[6] The Hudson Bay basin is the largest of the Paleozoic intracratonic basins of North America. The basin is situated within the region of Laurentia currently undergoing postglacial rebound. Sedimentary infill of the Hudson Bay basin is up to 2 km in thickness and consists of a thick Ordovician to Devonian section overlain by thin Cretaceous and Quaternary sections [*Hanne et al.*, 2004]. The Hudson Bay basin is underlain by several rift structures that appear to have been active during sediment deposition in the basin. *Hanne et al.* [2004] hypothesize that the subsidence of the Hudson Bay basin occurred due to this rifting. However, it is also possible that a high-density region in the uppermost mantle is currently depressing the Hudson Bay basin dynamically. The primary difficulty in determining the magnitude and nature of this dynamic force has been separating its geophysical signature from that of the large-scale postglacial rebound [*Tamisiea et al.*, 2007].

[7] The Congo basin is much older, larger and deeper than the Chad basin, and, despite its close proximity to the Chad, bears a greater resemblance to the Paleozoic intracratonic basins of North America. Covering an area of $1.2 \times 10^6$ km$^2$, roughly the size of Hudson Bay, the Congo is among the largest intracratonic basins. The basin straddles the equator in central Africa and is contained within the Congo craton, an amalgamation of crustal blocks that formed during the Proterozoic [*De Waele et al.*, 2008]. The seismically determined crustal thickness of the Congo craton is within the range 30–45 km with thickest crust observed beneath the Congo basin [*Pasyanos and Nyblade*, 2007]. Sediment infill of the basin is up to 9 km and consists of several unconformity-bounded packages that date in age from late Proterozoic to Quaternary [*Daly et al.*, 1992]. This pattern is similar to that observed in other intracratonic basins and indicates multistage basin development. The majority of these sediments are proposed to have been deposited in response to thermal contraction after a late Proterozoic rifting event. However, since the latest Jurassic or earliest Cretaceous the basin has been subsiding by an unknown mechanism.

[8] Using gravity data acquired during the Gravity Recovery and Climate Experiment (GRACE) [*Tapley et al.*, 2005] and topography from the Shuttle Radar Topography Mission (SRTM) [*Farr et al.*, 2007], we reexamine the admittance (an estimate of the linear transfer function between topographic and gravitational spectra; Appendix A) of the Congo basin. The admittance estimates obtained using these data imply that the topography of the Congo basin is dynamically supported. Using active source seismic data [*Daly et al.*, 1992], we construct a new isopach of the anomalous early Cretaceous to Quaternary sediments. This isopach is used to correct the SRTM data to highlight the topographic structure of the anomalous subsidence of the Congo basin, which we hypothesize has a dynamic origin. We then present three-dimensional models of the instantaneous dynamics of the cratonic Congo basin, calculated using the convection code CitcomT [*Billen et al.*, 2003], which are constrained using this anomalous topography and gravity. We discuss the compatibility of these models with the deeper seismic velocity structure beneath the Congo as revealed by tomography. Our models demonstrate that the Cretaceous-Quaternary anomalous subsidence of the Congo basin results from viscous support of a high-density region in the uppermost mantle. The preferred location of this anomaly is at 100 km depth with a maximum density anomaly of 27–60 kg m$^{-3}$. The location of this anomaly within the uppermost mantle, however, makes it difficult to uniquely determine the viscosity structure of the Congo lithosphere.

## 2. Previous Studies of the Cratonic Congo Basin

[9] The Congo basin is located almost entirely within the Democratic Republic of the Congo with its northern and northwestern extents reaching into the Republic of the Congo and the Central African Republic. It is one of the least studied intracratonic basins due to its relative inaccessibility and long-term regional political instability. Geological study during colonial (pre-1960) times largely consisted of geological mapping [*Cahen*, 1954] with some preliminary geophysics [*Évrard*, 1957] and the drilling of two exploratory boreholes [*Cahen et al.*, 1959, 1960]. The major results of this colonial work are summarized by *Giresse* [2005]. Since 1960, geological study of the Congo basin has largely been carried out by oil exploration companies and is proprietary. However, *Daly et al.* [1992] present an interpretation of seismic and well data collected in the early 1980s. Much of our current knowledge of the Congo basin's tectonic history is reliant upon interpretation of these seismic and well data.

[10] The Congo basin developed in stages. These stages are represented by four Paleozoic unconformity-bounded sedimentary sequences capped by a ~1–2 km thick late Jurassic/early Cretaceous to Quaternary sediment package [*Daly et al.*, 1992]. The oldest sedimentary rocks in the basin are late Proterozoic. It is not clear if rifting on the basin's basement faults predated or was coincident with deposition of the lowest sedimentary package. It is clear, however, that motion on these faults was reversed in response to collisional events related to the formation of Gondwana during the early and late Paleozoic [*Daly et al.*, 1991]. The evidence for these two collisional events is deformed, basinal sediments that are truncated by the sequence bounding unconformities. *Daly et al.* [1992] cite thermal relaxation after a late Proterozoic rifting event as the primary mechanism driving subsidence during deposition of the lower four stratigraphic packages. Since the early Mesozoic, the Congo craton has remained stable, with no internal collisional or rifting events taking place, making it difficult to determine the subsidence mechanism of the early Cretaceous to Quaternary basin sediments. *Sahagian* [1993] tentatively proposes a passive sediment catchment model

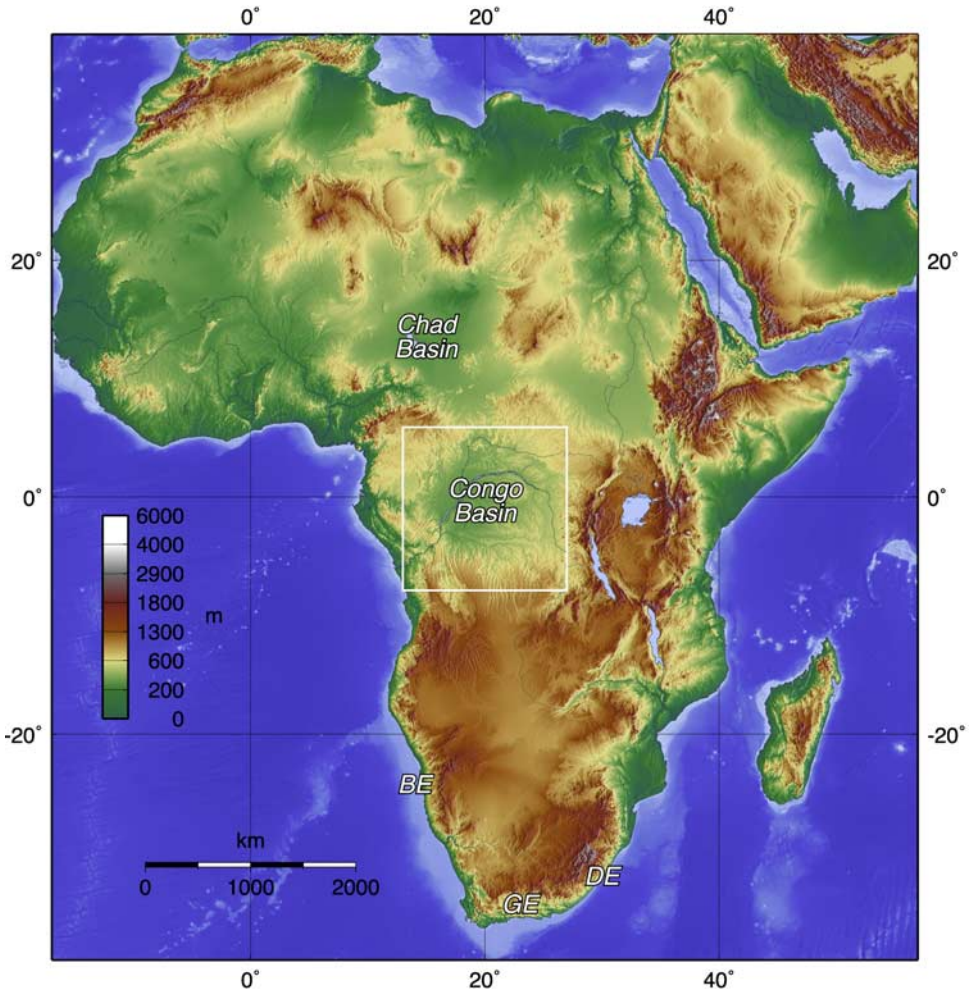


**Figure 1.** Base map showing the SRTM topography of Africa. The major features discussed in the text are labeled. Note the nearly circular depression of the Congo basin. The white box outlines the location of Figures 6 and 8. The south African escarpments are labeled DE, Drakensberg Escarpment; GE, Great Escarpment; and BE, Gamsberg Escarpment.

for this latest deposition within the basin, similar to that proposed by *Burke* [1976] for the Chad.

[11] The lithosphere underlying the Congo basin is being compressed between the East African Rift Zone and the Mid-Atlantic Ridge as evidenced from earthquake focal mechanisms [*Ayele*, 2002]. The state of stress in the North American craton during the periods of active subsidence in the Michigan, Williston and Illinois basins is also thought to be compressional, as evidenced by the correlation of basin subsidence with orogenic events [*Sloss*, 1988]. Other geophysical characteristics of the Congo basin are not typical of intracratonic basins. *Hartley and Allen* [1994] observe a long-wavelength Bouguer gravity low over the Congo. This gravity anomaly in combination with the long-wavelength topographic expression of the Congo basin gives large admittance values at long wavelengths, yielding an effective elastic thickness (EET) of 101 km for the lithosphere beneath the Congo basin [*Hartley and Allen*, 1994; *Hartley et al.*, 1996]. This estimate, while similar to estimates of EET in other cratonic regions, may only be an upper bound on the true elastic thickness of the Congo lithosphere [*McKenzie and Fairhead*, 1997]. Nevertheless, the ~2000 km wavelength of the Congo basin suggests that flexural support is not the primary mode of compensation for its topographic expression. *Hartley and Allen* [1994] suggest that the anomalous gravity and topography of the Congo basin results from the action of a downward dynamic force on the base of the lithosphere caused by convective downwelling in the mantle.

## 3. Observations and Data

### 3.1. Gravity

[12] The free-air anomaly gravity of Africa, derived from the GRACE satellite-only geopotential model GGM02S [*Tapley et al.*, 2005], expanded out to degree $l = 110$ ($\lambda \approx$ 362 km) shows that the Congo basin is coincident with an approximately 70 mGal free-air gravity low (Figure 2a). This gravity low is the dominant feature of continental Africa's gravity field. A geoid height anomaly calculated from GGM02S for the same wave band (Figure 2b) is coincident with the Congo basin, but the correlation is less dominant than evidenced in the free-air anomaly; the Congo

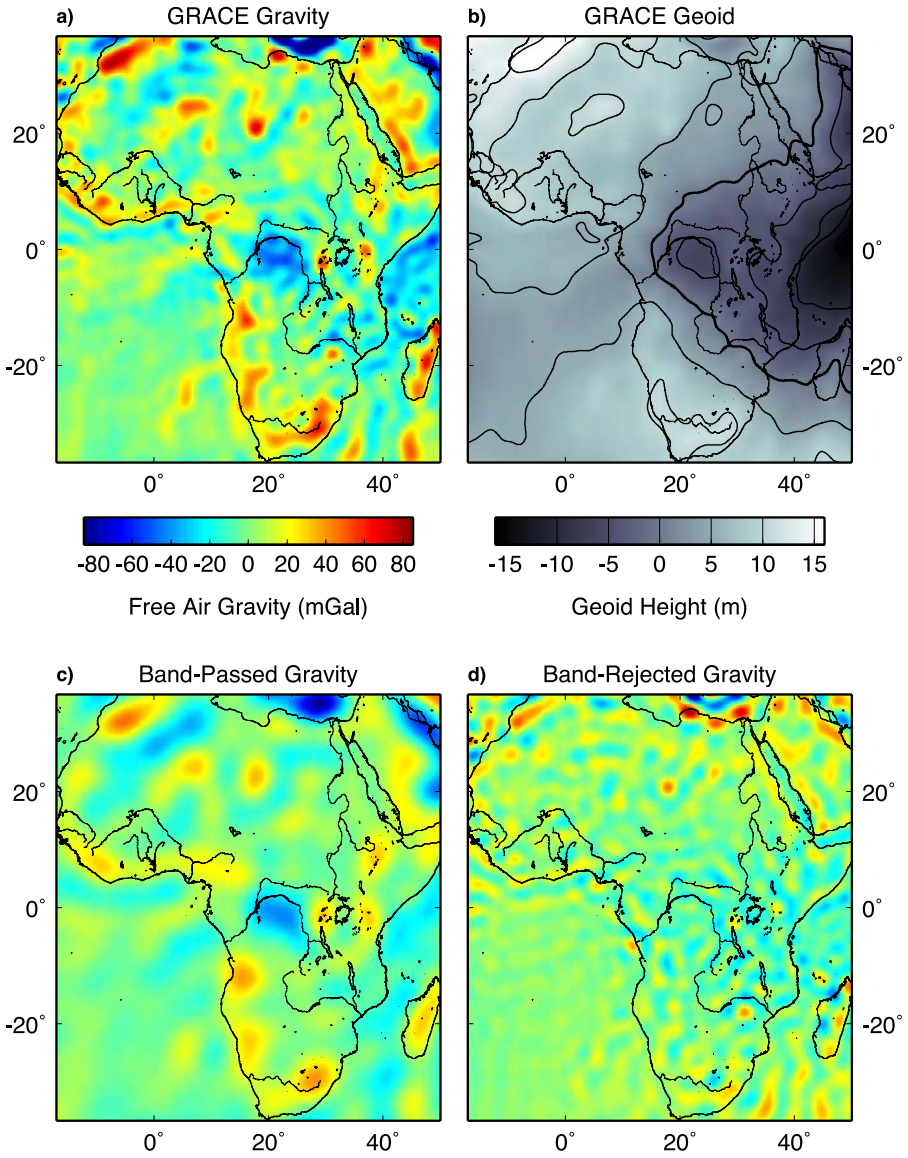


**Figure 2.** (a) Free-air gravity anomaly (GGM02S from GRACE) expanded to $L_{max}$ = 110. Note the prominent low coincident with the Congo basin. (b) Geoid heights from GGM02S. The Congo basin is coincident with an embayment in the high-amplitude, long-wavelength Indian geoid low. Contour interval is 5 m, with the zero contour as a thick line. (c) Filtered free-air anomaly (GGM02S) using a trapezoidal band pass filter ($l$ = 5-10-45-60). (d) Same as Figure 2c except the field was filtered using the conjugate band reject filter: Figures 2c and 2d represent a decomposition of the field in Figure 2a. Note that the gravity low associated with the Congo is contained within the wave band of anomalously high RMS amplitude highlighted in Figure 3a.

basin is coincident with an embayment in the longer wavelength Indian geoid low. The Hudson Bay Basin is coincident with a 60 mGal free-air gravity low; however, the spatial extent of this low is much larger than the basin, and it is difficult to separate the component of the gravity anomaly due to the basin from the postglacial rebound component [*Tamisiea et al.*, 2007].

[13] In order to explore the nature of the Congo gravity anomaly we examine the free-air gravity spectrum using a spatiospectral localization technique [*Simons*, 1996; *Simons et al.*, 1997]. The basis of this localization scheme is a windowing function centered at a specific geographic location and derived from a spherical cap, a function on the surface of the sphere whose magnitude equals one within a specified angular radius from its central location and zero outside that radius. The spectrum of this windowing function is given by truncating the spectrum of spherical cap of radius $\theta_c$ at a maximum spherical harmonic degree of $L_{win}$. $\theta_c$ is given by

$$\theta_c = \frac{\pi}{\sqrt{l_s(l_s+1)}}, \tag{1}$$

where $l_s = l/f_s$ is the ratio of the spherical harmonic degree of interest to a real-valued scaling factor $f_s \geq 1.0$. $L_{win}$ is

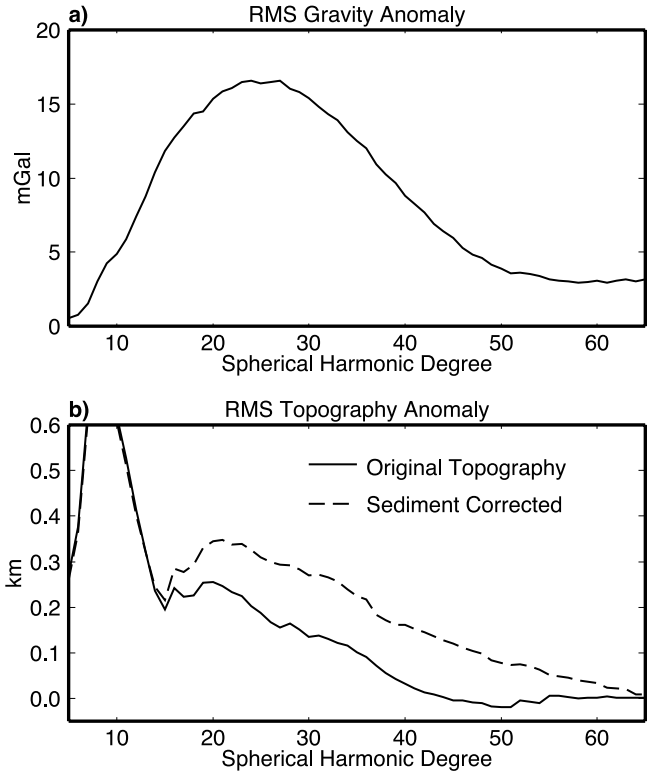


**Figure 3.** (a) Anomalous RMS amplitude spectrum of the GGM02S free-air gravity anomaly localized near the center of the Congo basin at 22.0°E, 1.75°S. The amplitude of the gravity anomaly near the Congo is particularly large within the wave band $10 < l < 45$. (b) Same as Figure 3a except that the RMS amplitude anomaly of the topography has been localized near the Congo; topography before the removal of the anomalous Mesozoic-Quaternary isopach (solid line); anomalous RMS amplitude of the topography after correction for sediment removal (dashed line). Note that there are two wave bands over which the topography of the Congo is anomalous. For the wave band $5 < l < 15$, the large amplitudes result from the spectral expression of the continent-ocean boundary, while the anomalous amplitudes within the wave band $15 < l < 45$ result from the topographic expression of the Congo basin. Sedimentation within the basin has preferentially dampened the topography within the wave band $15 < l < 65$, with uniform damping over $20 < l < 50$.

given by $L_{win} = \lceil l_s \rceil$ where $f(x) = [x]$ is the ceiling function. The Nyquist condition for this windowing process is given by

$$L_{Nyq} = L_{obs} - L_{win}. \tag{2}$$

where $L_{\mathrm{obs}}$ is the maximum spherical harmonic degree of the observations. Two schemes for choosing $f_{\mathrm{s}}$ have been used. *McGovern et al.* [2002] chose $f_{\mathrm{s}}$ proportional to $l$ so that $l_{\mathrm{s}}$ is constant, implying that $\theta_{\mathrm{c}}$ and $L_{win}$ are also constant. This choice results in a constant windowing function for all spherical harmonic degrees, most suitable for analyzing a particular geographic region. This windowing scheme has a constant spatial resolution, but a spectral resolution that increases with $l$. The Nyquist condition (2) for this windowing scheme, along with the bounds on $f_{\mathrm{s}}$ restricts the wave band over which this scheme can be applied to

$$L_{win} \leq l \leq L_{obs} - L_{win}. \tag{3}$$

*Simons et al.* [1997] use a different scheme for the windowing process in which $f_{\mathrm{s}}$ is constant for all windows, and as a result, window size varies with spherical harmonic degree, $l$. This scheme highlights the physical meaning of $f_{\mathrm{s}}$, namely, that it is the number of wavelengths contained within the windowing function. This scheme is well suited to analyzing large bandwidth signals. For different $l$, the wavelength varies and the window size is dilated so that the spectral resolution remains constant and spatial resolution increases with $l$. The Nyquist condition for this windowing scheme is

$$L_{Nyq} = \frac{f_s}{f_s + 1} L_{obs}. \tag{4}$$

These two windowing schemes are analogous to standard localized spectral analysis methods commonly used to analyze functions in the plane. The *McGovern et al.* [2002] scheme is similar to the 2-D isotropic short-time Fourier transform, while the dilations of the window used in the scheme of *Simons et al.* [1997] are similar to the dilations of the 2-D isotropic wavelet transform. By windowing a spherical harmonic field near a given location using this method we can then apply standard spectral analysis techniques in a localized sense.

[14] The anomalous root-mean-square (RMS) amplitude spectrum of the GGM02S free-air gravity anomaly localized near the Congo basin at 22.00°E, 1.75°S is calculated by subtracting the globally averaged local RMS amplitude spectrum of the free-air gravity from the RMS amplitude spectrum localized near the Congo (Figure 3). We utilize the windowing scheme of *Simons et al.* [1997] with a scaling factor, $f_{\mathrm{s}} = 1.5$. The free-air gravity near the Congo has anomalously large amplitudes throughout wave band $10 < l < 45$ (880 km $< \lambda <$ 3817 km; Figure 3a). We use this spectral signature to design a filter that decomposes the GGM02S free-air gravity model into two parts. By using a band pass trapezoidal filter ($l$ = 5-10-45-60) and its corresponding band reject filter it can be seen that the large gravity low associated with the Congo basin is wholly contained within the wave band of anomalously high RMS amplitude (Figures 2c and 2d). Even though we are focused upon a particular geographic region, we use the windowing scheme of *Simons et al.* [1997], with $f_s = 1.5$, in preference to that of *McGovern et al.* [2002] throughout this paper. Because the Congo gravity anomaly has a large bandwidth, the window size required to analyze the longest wavelength components of the gravity anomaly is much larger than that required to analyze the shortest wavelength components. Were we to choose a window large enough to analyze the entire signal, we would have poor spatial resolution at the shortest wavelengths of the gravity anomaly. Conversely by choosing a smaller window we would be

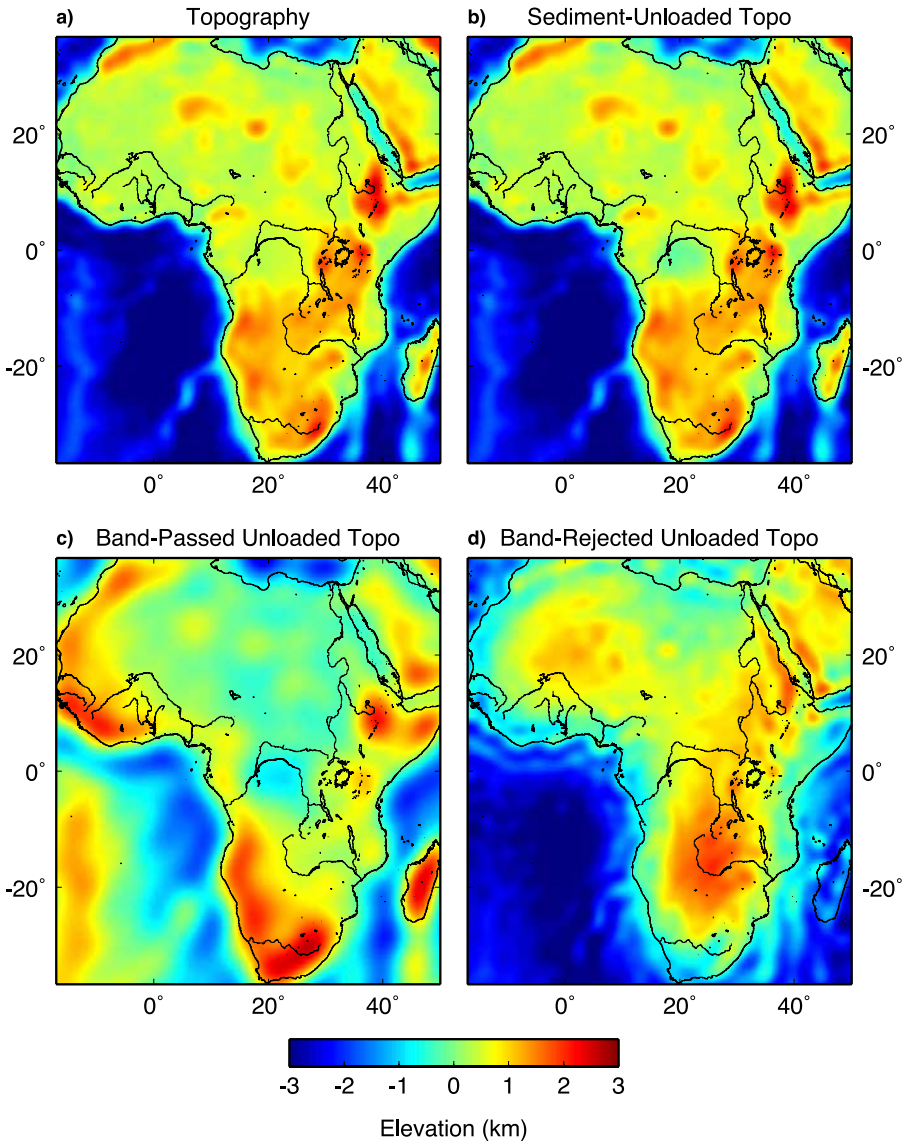


**Figure 4.** (a) Topography of Africa expanded out to $L_{max}$ = 110. The Congo basin has only a slight topographic expression. (b) Topography of Africa after the removal and unloading of the anomalous Mesozoic-Quaternary sedimentary infill of the Congo basin. Removal of these sediments highlights the structure of the Congo's anomalous topography which is nearly circular in shape. (c and d) Similar to the free-air anomaly of the Congo, this unloaded topography is also band limited as shown by decomposing the topography using an $l$ = 10-15-45-60 trapezoidal band pass and conjugate band reject filter.

gaining spatial resolution at the expense of not being able to analyze the entire bandwidth of the gravity anomaly. The windowing method of *Simons et al.* [1997] provides a compromise between these two extremes.

### 3.2. Topography

[15] The use of a global topographic model in which bathymetry is calculated by downward continuation of oceanic gravity anomalies, when comparing the spectral content of gravity and topography, will bias any estimation of the transfer function between gravity and topography to that of the downward continuation operation. This bias is easily avoided by using only ship track bathymetric measurements in the construction of a global topography model. We construct a new spherical harmonic representation of topography based upon the equivalent rock topography model ERT360 [*Pavlis and Rapp*, 1990] over oceanic regions. The ERT360 model, although dated, was created using only ship track bathymetric measurements for oceanic areas and is at sufficient resolution for our purposes. Over continental regions we use the SRTM topography data (Figure 1) for the construction of our model. Within this topographic model (expanded out to $l$ = 110; Figure 4a), the Congo basin is outlined as a subtle depression in the topography which is not as anomalous as the Congo basin's gravity signature at these long wavelengths (see Figure 2).

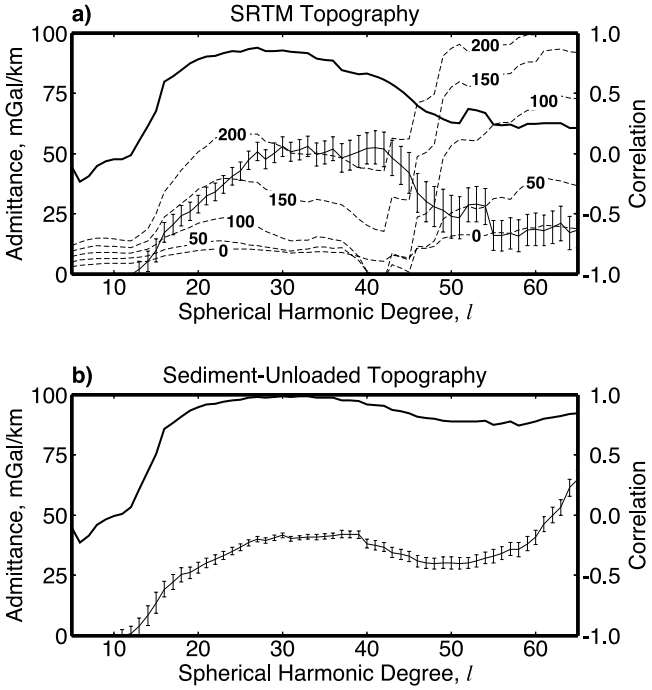


**Figure 5.** (a) Estimated admittance of the Congo basin localized near 22.00°E, 1.75°S (solid line with error bars), along with the localized correlation coefficient (thick line). The dashed lines are model admittances calculated assuming flexural support of a topographic load using the values listed in Table 1 and are labeled with the magnitude, in km, of the elastic thickness. The admittance of the Congo region is consistent with unreasonably large values of elastic thickness, indicating that the topography near the Congo is not maintained by lithospheric flexure. (b) Same as Figure 5a except that the sediment unloaded topography has been used in the admittance estimate.

However, the topographic depression of the basin is almost circular in shape, a characteristic which is unique within Africa.

[16] We again use the spectral localization method to calculate the RMS amplitude spectrum of the topography localized near the Congo basin (Figure 3b). The wave band $15 < l < 45$ (880 km $< \lambda <$ 2580 km) exhibits anomalous RMS topography whose amplitude peaks near $l = 20$ ($\lambda =$ 1950 km) and decays to 0 at $l = 40$ ($\lambda =$ 990 km). The RMS topography anomaly within the wave band $l < 15$ is much larger in amplitude. These large amplitudes result from the spectral expression of the extreme topographic variations associated with the ocean-continent boundary, especially the sudden transition from the high elevation of southern Africa to the ocean floor at the location of the south African escarpments (Figure 1). The spectra of step-like features such as the continent-ocean boundary exhibit large amplitudes at all degrees. At $l > 15$ our windowing functions are small enough that these transitions are masked out of the data and therefore do not affect our spectral estimates. However, at the longest wavelengths our spatial windows become large and these features begin to dominate the spectrum of the topography.

### 3.3. Admittance Between Gravity and Topography

[17] The topography and gravity data sets described above are significant updates to the regional data sets used by *Hartley and Allen* [1994] and *Hartley et al.* [1996] in their analyses of the gravitational admittance of the Congo. These analyses also relied upon admittance spectra calculated using Bouguer gravity anomalies in their estimates of the EET of the Congo lithosphere. *McKenzie and Fairhead* [1997] warn that EET estimates based on Bouguer admittance can only be considered upper bounds to the true EET, due to the effect of erosional damping on short-wavelength components of the topography. It is prudent therefore to reestimate the admittance spectrum of the Congo using our new data sets to verify the conclusions of *Hartley and Allen* [1994] and *Hartley et al.* [1996]. Since our data sets are global in scope, we again utilize spatiospectral localization to restrict our admittance analysis to the Congo region.

[18] We estimate the localized admittance near the center of the Congo basin, using the same windowing scheme as described above for our estimation of the anomalous RMS amplitude spectra of gravity and topography (Figure 5a; see Appendix A for details). There is relatively good correlation between the localized gravity and topography over the wave band $15 < l < 40$ (990 km $< \lambda <$ 2580 km), a wave band which also contains much of the power of the anomalous free-air gravity. Throughout this wave band the estimated admittance is >25 mGal km$^{-1}$; the admittance is relatively constant at ~50 mGal km$^{-1}$ for $25 < l < 40$. For comparison with the results of *Hartley and Allen* [1994] and *Hartley et al.* [1996], we calculate synthetic gravity spherical harmonic coefficients assuming that the lithosphere responds elastically to the topographic load. In this model, the synthetic gravity has two sources, the gravity anomaly caused by the topography and that caused by the flexural deflection of the Moho:

$$g^F_{lm} = g^H_{lm} + \left(\frac{R_E - T_c}{R_E}\right)^l g^W_{lm}, \tag{5}$$

where the superscripts $H$ and $W$ indicate the spherical harmonic coefficients of gravity associated with the topography and Moho deflection, respectively. For the subtle topography of the Congo region the gravity coefficients on the right hand side of (5) can be approximated by

$$g^H_{lm} = 4\pi\Delta\rho_H G \frac{l+1}{2l+1} h_{lm} \tag{6}$$

$$g^W_{lm} = 4\pi\Delta\rho_M G \frac{l+1}{2l+1} w_{lm}. \tag{7}$$

$\Delta\rho_M$ and $\Delta\rho_H$ are the density contrasts across the topographic and Moho interfaces, respectively, and $G$ is the gravitational constant. Coefficients of Moho deflection $w_{lm}$ are calculated using the formulation for the flexural

**Table 1.** Parameters Used in Flexure Calculations

| Variable | Symbol | Value |
|---|---|---|
| Crustal thickness | $T_C$ | 35 km |
| Earth radius | $R_E$ | 6371 km |
| Topographic density contrast | $\Delta\rho_H$ | 2670 kg m$^{-3}$ |
| Moho density contrast | $\Delta\rho_M$ | 630 kg m$^{-3}$ |
| Gravitational acceleration | $G$ | 9.81 m s$^{-2}$ |
| Young's modulus | $E$ | 100 GPa |
| Poisson's ratio | $\nu$ | 0.25 |

deflection of a thin spherical elastic shell [*McGovern et al.*, 2002; *Turcotte et al.*, 1981]:

$$w_{lm} = -\left(\frac{\Delta\rho_H}{\Delta\rho_M}\frac{l(l+1)-(1-\nu)}{\sigma\left(l^3(l+1)^3-4l^2(l+1)^2\right)+\tau(l(l+1)-2)+l(l+1)-(1-\nu)}\right)h_{lm}, \quad (8)$$

where

$$\sigma \equiv \frac{\tau}{12(1-\nu^2)}\left(\frac{T_e}{R_E}\right)^2 \quad (9)$$

and

$$\tau \equiv \frac{ET_e}{R_E^2 g\Delta\rho_M}. \quad (10)$$

$T_e$ is the thickness of the elastic shell, $E$ is Young's modulus, $g$ is the acceleration of gravity, and $\nu$ is Poisson's ratio. We use equations (5)–(10) and the parameters listed in Table 1 to calculate synthetic gravity coefficients for values of the elastic thickness $T_e$ = 0, 50, 100, 150 and 200 km. We then estimate the localized admittance between the topography and these synthetic gravity fields near the Congo at 22.00°E, 1.75°S (Figure 5a).

[19] While the overall fit of the admittance estimated using the GRACE gravity with the synthetic admittances is poor, the magnitude of the former is consistent with flexural models with $T_e$ > 100 km over almost all of the wave band of good correlation between gravity and topography (Figure 5a). The plateau of ~50 mGal km$^{-1}$ admittance for the 25 < $l$ < 40 wave band is consistent with $T_e$ ~ 200 km. The average magnitude of the Congo's admittance at long wavelengths (Figure 5a) is consistent with the $T_e$ value of 101 km estimate of *Hartley and Allen* [1994] and *Hartley et al.* [1996]. In general, continental regions exhibit $T_e$ values much smaller than this, generally less than 25 km [*McKenzie*, 2003]. The unreasonably large $T_e$ required to fit the modeled admittance to the GRACE admittance indicates that lithospheric flexure is not an important mode of compensation of the Congo topography. We agree with the conclusion of *Hartley and Allen* [1994] that there is likely a downward dynamic force, resulting from mantle convection, acting on the base of the Congo lithosphere. Furthermore we hypothesize that surface subsidence caused by mantle convection resulted in the deposition of the anomalous Mesozoic-Quaternary strata identified by *Daly et al.* [1992].

### 3.4. Cretaceous-Quaternary Basin Infill

[20] In order to highlight the pattern of Congo basin dynamic subsidence we remove the anomalous late Cretaceous to Quaternary sediments from the topography. The removal process involved is similar to that of back stripping [e.g., *Watts and Ryan*, 1976]: remove the sedimentary basin infill from the topography by unloading its mass from the lithosphere assuming a compensation model.

[21] We reinterpret the seismic data of *Daly et al.* [1992] with well control provided by the SAMBA and DEKESE wells [*Cahen et al.*, 1959, 1960] and the 1981 Gilson well to constrain the shape of the Mesozoic-Quaternary isopach (Figure 6). Time-depth conversions were performed using the refraction velocities determined at the SAMBA well by *Évrard* [1957]. The lateral extent of these rocks was constrained by digitizing outcrop limits of the isopach from the UNESCO International Geologic Map of Africa [*Commission for the Geological Map of the World*, 1987] (Figure 6). We then fit a smooth surface to these data using the MATLAB® gridfit subroutine (J. D'Errico, Surface fitting using gridfit, 2005, available from MATLAB® Central at http://www.mathworks.com/matlabcentral). The isopach map of these sediments shows they are oval in shape and reach ~1200 m in thickness (Figure 6). The region of significant sediment accumulation (>50 m) measures ~1200 km east-west and 900 km north-south and is coincident with the location of the Congo free-air anomaly. As is typical of the sediment fill of intracratonic basins there is no evidence of significant sediment deformation in the seismic data.

[22] In order to refine our estimate of the dynamic component of topography, we unload the anomalous isopach from the SRTM topography. Given the large area covered by these sediments we assume local compensation in which the corrected topography is given by

$$H_{Corrected} = H_{SRTM} + \left(\frac{\rho_s}{\rho_m} - 1\right)I, \quad (11)$$

where $\rho_s$ and $\rho_m$ are the bulk density of the sediment infill and mantle, respectively, and $I$ is the sediment thickness. The density of the sediment infill is constrained by lithology and burial depth. Analysis of the well data indicates that $\rho_s$ = 2000 kg m$^{-3}$, and we assume a mantle density of 3300 kg m$^{-3}$. Equation (11) gives a maximum topography correction of ~−475 m. We use the sediment-corrected SRTM topography to calculate a second spherical harmonic representation of topography and expand this corrected topographic field to $l$ = 110 (Figure 4b). For comparison with the uncorrected topography we calculate the anomalous RMS amplitude spectrum of this corrected topographic field (Figure 3b). As expected, given the large area covered by the anomalous sedimentary rocks, sedimentation in the Congo basin has

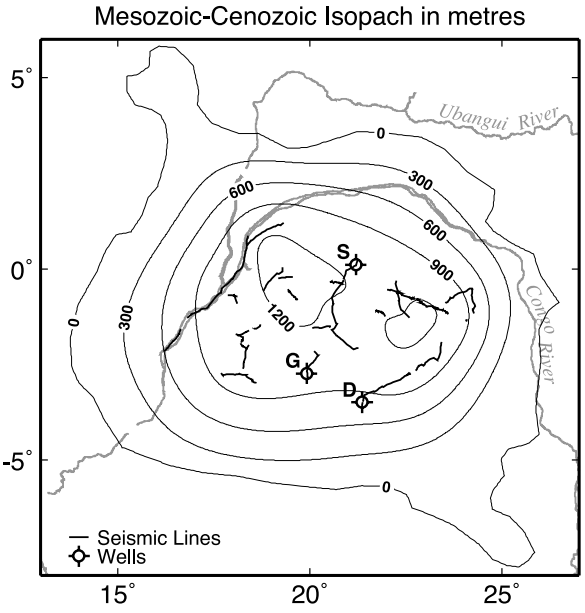


**Figure 6.** Contours of Mesozoic-Quaternary sedimentary rock thickness (thin black lines; labeled in m). See Figure 1 for location; the Congo and Ubangui rivers are shown as gray lines for reference. These sedimentary units are identified by *Daly et al.* [1992] as having no explainable subsidence mechanism. The location of thickest sediment infill is coincident with the location of the Congo gravity anomaly (Figure 2). The thick black lines and well symbols denote the locations of the seismic sections and wells used in the construction of this map. The wells are designated DEKESE (D), SAMBA (S), and Gilson (G). Velocities determined by refraction surveys near the location of the SAMBA well were used for time-depth conversion of the seismic data [*Évrard*, 1957].

preferentially dampened the topography over the wave band $15 < l < 65$ (610 km $< \lambda <$ 2580 km) with relatively constant damping occurring over $20 < l < 50$ (790 km $< \lambda <$ 1950 km). Topographic modification caused by sedimentation also appears to be partially responsible for the large admittance associated with the Congo basin. Estimating the admittance using the sediment-corrected topography in place of the SRTM topography decreases the admittance within the wave band of anomalous gravity by ~10 to ~40 mGal km$^{-1}$. Even after the sediments have been removed, however, the admittance remains too high to be explained by lithospheric flexure. Typical admittance values from cratonic regions are <20 mGal km$^{-1}$ at these wavelengths. Similar to the decomposition of the gravity into band-passed and band rejected components, we decompose the sediment-corrected topography into components using a similar trapezoidal filter ($l$ = 10-15-45-60; Figures 4c and 4d). While restricted to a slightly smaller wave band, this decomposition demonstrates that the sediment-corrected topography is not only spatially coincident with the Congo free-air gravity but spectrally coincident as well.

### 3.5. Tomographic Structure of Congo Lithosphere and Asthenosphere

[23] Global tomographic models of shear wave velocity anomaly [*Ritsema et al.*, 1999; *Mégnin and Romanowicz*, 2000; *Gu et al.*, 2001; *Grand*, 2002] generally agree on the velocity structure of the lithosphere and upper mantle beneath central Africa. Of these global models we choose S20RTS [*Ritsema et al.*, 1999; *Ritsema and van Heijst*, 2004] to be representative of the general pattern observed (Figure 7). This velocity structure consists of a region of approximately +5% maximum-amplitude shear wave velocity anomaly, relative to the Preliminary Reference Earth Model (PREM) [*Dziewonski and Anderson*, 1981], located at a depth of ~150 km beneath the Congo basin (Figures 7a, 7c, and 7d). The anomalous high-velocity region decays to +1% at ~300 km depth (Figures 7b, 7c, and 7d). Velocities consistent with PREM (0%) are reached at a much greater depth, ~800 km (Figures 7c and 7d). The horizontal extent of this region covers the entire Congo basin and is connected with a region of similar anomalous velocity beneath southern Africa (Figure 7a). In S20RTS, the Congo velocity anomaly forms a local maximum distinct from the velocity maximum beneath southern Africa.

[24] Regional models of the shear wave velocity anomaly beneath Africa, calculated using Rayleigh wave phase velocities, are not as consistent. *Ritsema and van Heijst*'s [2000] model was calculated using a subset of the data used in S20RTS, and exhibits a similar pattern of shear wave velocity anomaly, although resolution is poor at depths greater than 250 km. S. Fishwick (Seismic studies of the African continent and a new surface wave model of the uppermost mantle, paper presented at Workshop TOPOAFRICA, Géosciences Rennes, Rennes, France, 8 November, 2007) presents a model based on an updated data set relative to that of *Ritsema and van Heijst* [2000]. This data set was constructed with an emphasis on high-quality data and the resulting velocity structure is very similar to S20RTS. Both of these models indicate that shear wave velocity anomalies beneath central Africa are strongest beneath the Congo basin at a depth of 100–150 km. In contrast, the model of *Pasyanos and Nyblade* [2007] characterizes the upper mantle beneath parts of the Congo craton with anomalously high velocities; however, the region immediately below the Congo basin is not anomalous. *Pasyanos and Nyblade*'s [2007] model does indicate that the sediments of the Congo basin make up the upper 20% of a 45 km thick crust, the thickest observed on the African continent. *Pasyanos and Nyblade* [2007] interpret the absence of anomalously fast velocities in the upper mantle beneath the basin as indicative of a missing cratonic keel, proposing that the Congo basin overlies a hole in the cratonic mantle lithosphere. They attribute the difference between their model and previous models to poor horizontal resolution in the latter: the Congo basin is surrounded by anomalously fast lithosphere which, in these models, has been "smeared" into the upper mantle beneath the Congo basin. However, the lack of seismic stations within the Congo region is the primary limit on the resolution of tomographic inversions of the upper mantle beneath the Congo region. Until better station coverage is achieved, it will be difficult to accurately determine these velocities.

[25] Shear wave velocities are sensitive to temperature because of the strong temperature dependence of the shear modulus [*Priestly and McKenzie*, 2006]. As the temperature within the mantle approaches the melting temperature the

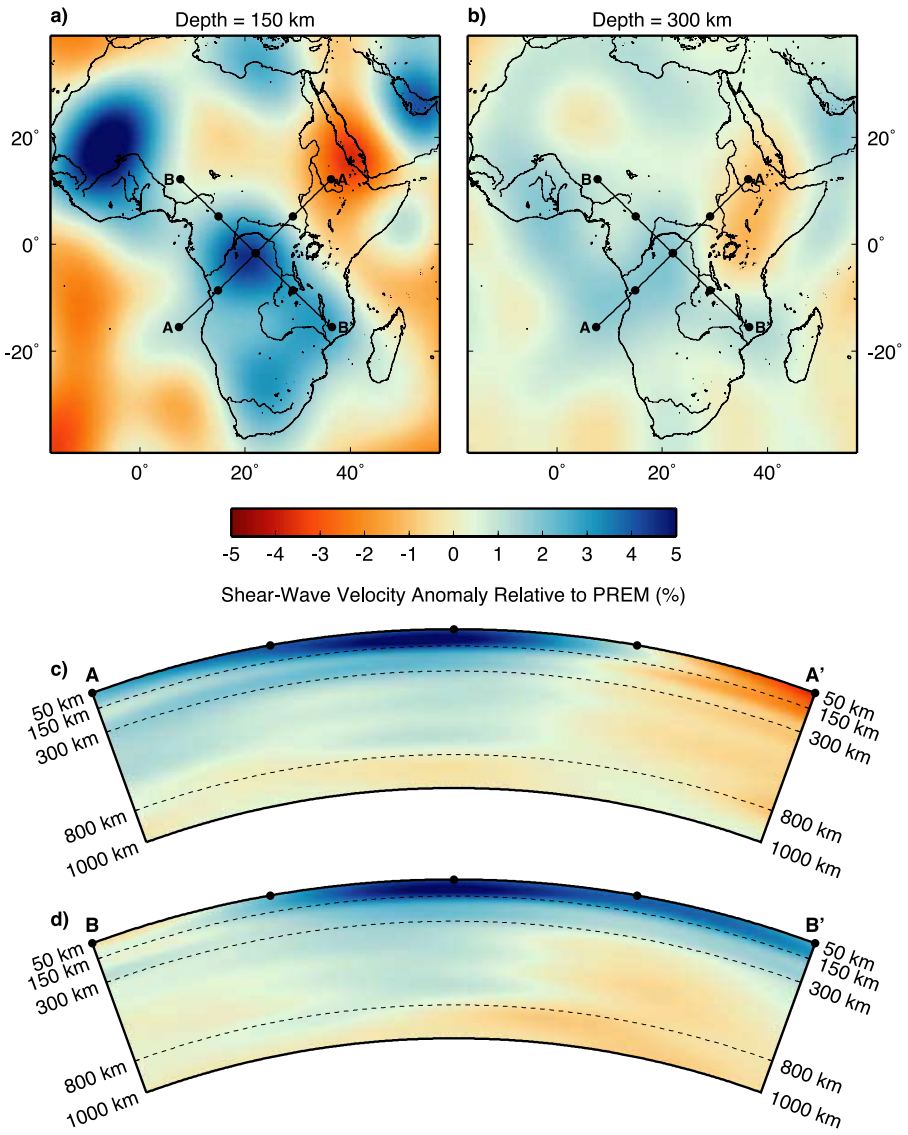


**Figure 7.** (a) Depth slice through the tomography model S20RTS [*Ritsema et al.*, 1999; *Ritsema and van Heijst*, 2004] at a depth of 150 km. Note the +5% shear wave velocity anomaly (relative to PREM) beneath the Congo basin which forms a maxima distinct from the fast regions beneath southern Africa. (b) Same as Figure 7a but at a depth of 300 km. At this depth the Congo velocity anomaly has magnitude +1%. (c) NE–SW cross section through S20RTS along the profile A-A′. (d) Same as Figure 7c, however, the cross section trends NW–SE along profile B-B′. These two cross sections highlight the depth extent of the Congo basin velocity anomaly. The maximum anomaly of +5% occurs near a depth of 100–150 km. This anomaly decays with depth to +2% over the depth range 150–300 km. From 300 to 800 km depth the velocity anomaly is relatively constant at 1%, reaching 0% near 800 km deep.

magnitude of the shear modulus is reduced and seismic velocities decrease. Temperature is also an important, but not exclusive, control on density throughout the mantle, with the coefficient of thermal expansion being $\sim 10^{-5}$ K$^{-1}$. Cold regions within the mantle are therefore denser and have greater shear wave velocities than their warmer surroundings. If the velocity anomaly beneath the Congo basin as shown in S20RTS is a robust feature, it may indicate the presence of an anomalously dense region in the upper mantle beneath the Congo, consistent with dynamic support of the Congo basin's anomalous topography. However, on the other hand, if the lack of high velocities beneath the Congo in *Pasyanos and Nyblade*'s [2007] model is verified, it does not necessarily contradict a high-density region within the upper mantle. *Anderson* [2007a, 2007b] points out that eclogitic phases within the uppermost mantle can have negative or zero shear wave velocity anomalies, but still be relatively dense compared to surrounding mantle. Thus the results of *Pasyanos and Nyblade* [2007] do not directly rule out the presence of a density anomaly beneath the Congo. Because of this conflict between models we do

not use the tomographic models as a direct constraint on our dynamic models.

## 4. Instantaneous Dynamics of the Cratonic Congo Basin

### 4.1. Dynamic Models of Cratonic Basin Subsidence

[26] Mantle dynamics has long been hypothesized to play a role in intracratonic basin subsidence. *DeRito et al.* [1983] demonstrated using semianalytical models of viscoelastic beam flexure, that stress changes in the lithosphere could cause anomalous high-density flexurally compensated bodies within the lithosphere to become unstable, flow, and essentially relax toward an isostatic state. Accompanying this flow is a depression of the surface, causing the formation or reactivation of subsidence in an intracratonic basin. *Middleton* [1989] presented a model in which intracratonic basin subsidence is caused by the combined effects of dynamic topography and thermal contraction over an asthenospheric downwelling or "cold spot." *Middleton* [1989] noted, however, that permanent subsidence resulting from this mechanism is difficult to achieve, requiring that a fraction of sediment be preserved above base level as the basin is uplifted in response to removal of the cold spot. Models of intracratonic basin subsidence caused by downward flow of dense eclogite bodies within the cratonic lithosphere roughly predict the subsidence histories of the Michigan, Illinois and Williston basins [*Naimark and Ismail-Zadeh*, 1995]. However, attempts at modeling the role of mantle dynamics in intracratonic sedimentary basin subsidence have had limited usefulness; inadequate observational constraint makes it difficult to uniquely determine model parameters.

[27] Geophysical and geological observations at the Congo basin provide a unique and unprecedented opportunity to study the role dynamic topography plays in cratonic basin subsidence. The correlation of the Congo gravity anomaly, anomalous topographic depression and upper mantle shear wave velocity anomaly is striking. Nowhere else are these quantities as well correlated at such large wavelengths. All three are present at the Hudson Bay basin but have much larger variation in spatial extent. At the Congo, these data combine to provide tight constraints on the dynamic processes currently depressing the Congo lithosphere.

### 4.2. Calculation of Model Topography and Gravity

[28] The observations outlined in section 3 only constrain the current state of the Congo basin. There is no information about the evolution of the basin contained in the gravity, topography or shear wave velocity anomaly associated with the basin. Therefore, following the approach of *Billen et al.* [2003], we calculate only the instantaneous dynamic topography.

[29] Under the infinite Prandtl number and Boussinesq approximations, the force balance between mantle density anomalies and surface deflection is governed by conservation of mass, as expressed by the continuity equation:

$$\vec{\nabla}\cdot\vec{u}=0 \tag{12}$$

and conservation of momentum as expressed by the Stokes equation:

$$\vec{\nabla}\cdot\tilde{\sigma}+\vec{\mathrm{f}}=\vec{0}, \tag{13}$$

where $\vec{u}$ is the velocity vector, $\tilde{\sigma}$ is stress and $\vec{\mathrm{f}}$ is the body force. The over arrow and over tilde notations indicate vectors and second-order tensors, respectively. We adopt a Newtonian-viscous constitutive relation:

$$\tilde{\sigma}=-P\tilde{\mathrm{I}}+\eta\dot{\tilde{\varepsilon}}, \tag{14}$$

in which $\tilde{\mathrm{I}}$ is the identity tensor, $P$ is pressure, $\eta$ is the dynamic viscosity and $\dot{\tilde{\varepsilon}}$ is the strain rate tensor defined as

$$\dot{\tilde{\varepsilon}}=\vec{\nabla}\vec{u}+\left(\vec{\nabla}\vec{u}\right)^{\mathrm{T}}. \tag{15}$$

The body force is given by

$$\vec{\mathrm{f}}=\rho_o\alpha(T-T_o)g\hat{\mathrm{r}}. \tag{16}$$

$T$ is absolute temperature, $T_o$ is a reference temperature, $\rho_o$ is a reference density, $\alpha$ is the coefficient of thermal expansion, and $\hat{\mathrm{r}}$ is the radial unit vector. Nondimensionalizing using the definitions

$$\begin{aligned}&\vec{u}=\frac{\kappa}{R_E}\vec{u}', \quad P=\frac{\eta_o\kappa}{R_E^2}P',\\ &\eta=\eta_o\eta', \quad \vec{\nabla}=\frac{1}{R_E}\vec{\nabla}', \quad T=T_o+\Delta TT',\end{aligned} \tag{17}$$

where $\kappa$ is the thermal diffusivity, $\eta_o$ is a reference viscosity and $\Delta T$ is the temperature difference between Earth's surface and the mantle's interior, yields from (12),

$$\vec{\nabla}'\cdot\vec{u}'=0, \tag{18}$$

and from the combination of (13)–(16),

$$-\vec{\nabla}'P'\tilde{\mathrm{I}}+\vec{\nabla}'\cdot\left(\eta'\vec{\nabla}'\vec{u}'+\eta'\left(\vec{\nabla}'\vec{u}'\right)^{\mathrm{T}}\right)+RaT'\hat{\mathrm{r}}=\vec{0}, \tag{19}$$

where the nondimensional Rayleigh number, $Ra$, is

$$Ra=\frac{\rho_o\alpha\Delta TgR^3}{\eta_o\kappa}. \tag{20}$$

$Ra$ is a measure of the relative importance of buoyancy and viscous resistance. Values of the parameters used in the models presented here give a Rayleigh number of $4.35\times10^8$ (Table 2).

[30] We solve equations (18) and (19) for $P'$ and $\vec{u}'$ in spherical coordinates using the finite element (FE) mantle convection code CitcomT [*Billen et al.*, 2003]. Our model domain consists of an 80° by 80° spherical sector centered on the equator whose depth ranges from the surface to 2890 km, the core-mantle boundary (CMB; Figure 8). The total number of elements in each dimension is 216. The grid spacing varies in latitude and longitude with the innermost

**Table 2.** Parameters Used in Viscous Models

| Variable | Symbol | Value |
|---|---|---|
| Reference density | $\rho_o$ | 3300 kg m$^{-3}$ |
| Temperature change across model | $\Delta T$ | 1300 K |
| Themal diffusivity | $\kappa$ | $1 \times 10^{-6}$ m$^2$ s$^{-1}$ |
| Coefficient of thermal expansion | $\alpha$ | $2 \times 10^{-5}$ K$^{-1}$ |
| Reference viscosity | $\eta_o$ | $5 \times 10^{20}$ Pa s |
| Rayleigh number | $Ra$ | $4.35 \times 10^8$ |

34° by 34° region having a constant grid spacing of 0.2° which increases linearly outside this inner region to 2.75° at the model boundaries. Depth grid spacing is 7 km over the uppermost 700 km, linearly increasing beneath to 40 km at the CMB. Boundary conditions are reflecting ($u_{\phi\phi} = 0$ or $u_{\theta\theta} = 0$ and $\sigma_{r\theta} = \sigma_{r\phi} = 0$) on the sidewalls of the model and free slip ($u_{rr} = 0$, $\sigma_{r\theta} = \sigma_{r\phi} = 0$) on the upper and lower surface. In addition, nondimensional temperature, $T'$, equals 0 on the upper surface and 1 at the CMB. The equatorial position of the model domain ensures its symmetry about the equator. For comparison with observations the results obtained on this domain are rotated, preserving north so that the center of the model domain coincides with the center of the Congo basin at 22.00°W, 1.75°S.

[31] CitcomT utilizes the consistent boundary flux (CBF) method [*Zhong et al.*, 1993] to calculate the normal stress on the upper surface of the model domain. Rather than attempt to calculate the normal stress on this surface, $\sigma_{rr}$, using the constitutive relation (14) the CBF method uses the solution to the model pressure and velocity fields ($P'$ and $\vec{u}'$) to solve the Stokes and continuity equations for the normal stress directly on the upper free surface of the model. *Zhong et al.* [1993] demonstrate that the CBF method is substantially more accurate, in terms of relative errors, than calculating the normal stress by smoothing element stresses on the free surface. *Billen et al.* [2003] benchmarked this procedure for the spherical problem solved by CitcomT.

[32] Dynamic topography is the topography that results in response to the normal stress imposed on the surface by viscous flow in the mantle. Because of the long wavelength of the anomalous topography observed in the Congo we adopt a model in which the surface-normal stress is balanced by topography at the Earth's surface:

$$H_M = \frac{\sigma_{rr}}{\Delta\rho_{fill} g}, \tag{21}$$

where $H_m$ is the model topography and $\Delta\rho_{fill}$ is the density contrast between the uppermost mantle and the material infilling the surface deflection. For our models, we compare this modeled topography to the sediment-corrected topography calculated in section 3 and therefore the infilling material is air and $\Delta\rho_{fill}$ is equal to the reference density $\rho_o$.

[33] The model gravity consists of two parts, the gravity due to the variations of density within the mantle and the gravity due to the mass deficit created by the dynamic topography. The spherical harmonic coefficients of the gravity at Earth's surface ($r = R_E$) due to the internal density structure, $\rho(r, \theta, \phi)$, are calculated using

$$g^I_{lm} = G \int_{R_{CMB}}^{R_E} \left(\frac{r}{R_E}\right)^{l+2} \frac{l+1}{2l+1} \int_\Omega \rho(r,\theta,\phi) Y^*_{lm}(\theta,\phi) d\Omega dr, \tag{22}$$

where $Y_{lm}(\theta, \phi)$ is a spherical harmonic (see Appendix A) and $d\Omega = \sin(\theta) d\theta d\phi$. The spherical harmonic coefficients and the integral over $r$ are calculated within CitcomT using the numerical quadrature method used in the FE computation. The topographic component of the gravity is calculated using a modified version of (22) in which the integral over $r$ and the upward continuation factor are dropped because the topographic density anomaly is located at the upper surface of the model. This density anomaly equals the model topography scaled by the surface density contrast $\Delta\rho_s$:

$$g^H_{lm} = G \frac{l+1}{2l+1} \Delta\rho_s h_{lm} = G \frac{l+1}{2l+1} \int_\Omega H_M(\theta,\phi) Y^*_{lm}(\theta,\phi) d\Omega, \tag{23}$$

where $h_{lm}$ are the spherical harmonic coefficients of the model topography, $H_M$. The magnitudes of these two components of gravity are similar and opposite in sign because a positive density within the mantle causes a negative density anomaly at the surface. The total gravity anomaly is therefore relatively small in magnitude compared to either the gravity from internal density variations or the surface deflection and therefore these two gravity components must be calculated as accurately as possible. The consistent boundary flux method therefore also facilitates accurate calculation of the model gravity anomaly.

### 4.3. Model Setup

[34] The shape of the input density structure of our models is described by a cylindrically symmetric bivariate Gaussian density anomaly at a specified depth (Figure 9a). The axis of symmetry is vertically oriented beneath the center of the Congo basin at 22.00°E, 1.75°S. The horizontal width and vertical thickness of these anomalies is specified by their half width and half thickness (the distance at which the magnitude of the Gaussian drops to one-half maximum). The half width is measured along the surface of

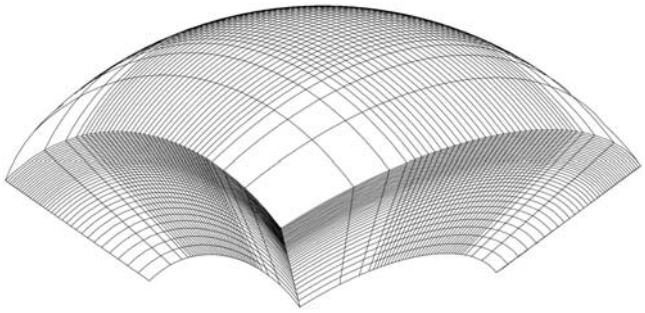

**Figure 8.** A 3-D view of our finite element mesh viewed from the southeast. The gridlines have been decimated by a factor of 6 for clarity. The domain extends from the CMB to the surface, spans 80° longitude by 80° latitude and straddles the equator. The total number of nodes in each dimension is 217. The central 34° by 34° region has a grid spacing of 0.2° increasing linearly outside this region to 2.75° at the edge of the domain. In depth the grid spacing is 7 km over the uppermost 700 km of the mantle and increases linearly below to 40 km spacing at the CMB.

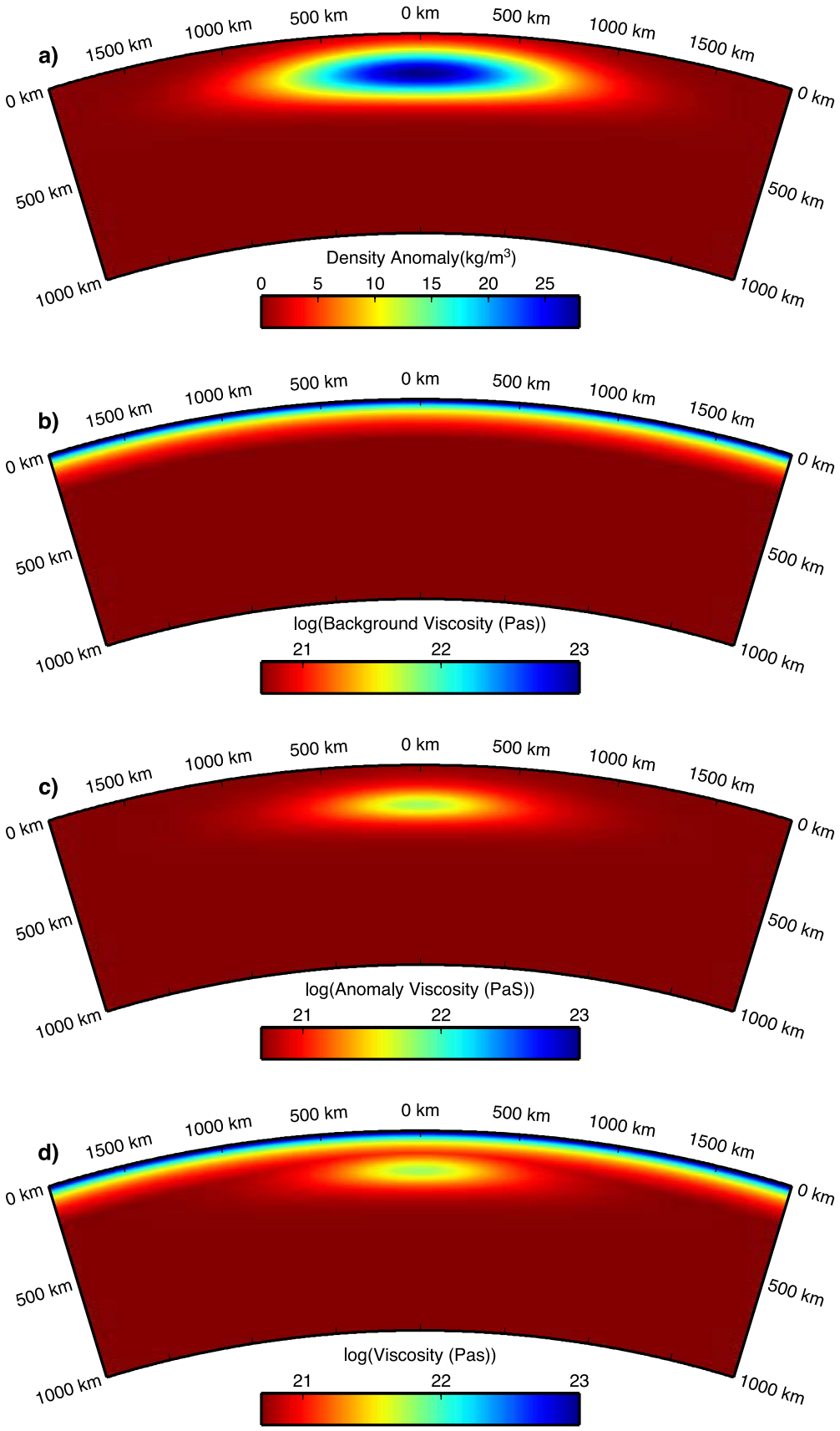
a)
0 km
500 km
1000 km
1500 km
Density Anomaly(kg/m3)
0 5 10 15 20 25
b)
log(Background Viscosity (Pas))
21 22 23
c)
log(Anomaly Viscosity (PaS))
21 22 23
d)
log(Viscosity (Pas))
21 22 23

**Figure 9**

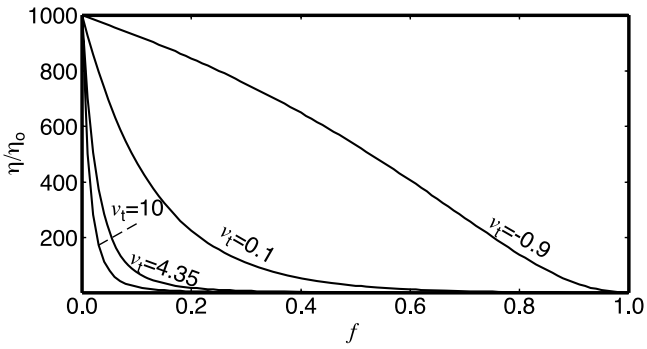


**Figure 10.** Viscosity as a function of $f$ for various values of $v_T$ and $r = 1000$. For the background viscosity, $f$ equals the ratio of depth to lithospheric thickness. This viscosity profile is nearly linear with $f$ for $v_T = -0.9$, nearly exponential for $v_T = 0.1$ and superexponential for $v_T = 4.35$ and 10.

the Earth so that deeper models, while having a smaller absolute width, have the same angular width as shallower models. Thus the shape of these density anomalies, when the half thickness is less than the half width is an oblate spheroid. In general, we run these models in groups containing 21 members of constant width whose depth location varies from 50 to 500 km and whose half thickness at each depth varies from 50 km to a maximum equal to their depth. The magnitude of the maximum density anomaly of each group member is varied so that the total anomalous mass of each member is constant within a group.

[35] The viscosity of our models is described using the relation

$$\eta = \eta_o \exp\left(\ln(r)\frac{1 - f(\vec{x})}{1 + v_T f(\vec{x})}\right), \tag{24}$$

in which $f$ [0, 1] is a function of position $\vec{x}$, $r$ is the ratio of maximum to minimum viscosity, and $v_T$ describes the decay of viscosity with increasing $f$ (Figure 10). This relation is similar to that used by *Conrad and Molnar* [1999] in which nondimensional temperature has been replaced by $f$ and to which we have added the parameter $v_T$. For the background viscosity, $f$ equals the ratio of depth to lithospheric thickness within the lithosphere and equals 1 throughout the sublithospheric mantle (Figure 9b). The viscosity of the density anomalies is calculated using the same bivariate Gaussian geometry to describe the spatial distribution of $f$. The maximum viscosity of the anomalies is expressed in terms of the depth at which the maximum viscosity equals the background viscosity, symbolized $\eta_{eqv}$ depth and expressed in km (in Figure 9c, $\eta_{eqv}$ depth = 50 km, so the maximum viscosity of the anomaly equals the background viscosity in Figure 9b at 50 km depth). The viscosity at any given location is taken to be the larger of the background and anomalous viscosities (Figure 9d). Within each group of models we use the same viscosity parameters and background viscosity. This is done to ensure that while the mass distribution of each group member may be different, its mass remains mechanically coherent. In addition we explore the effects of a viscosity increase beneath the lithosphere by specifying, for some models, a transition depth where the viscosity increases by a specified ratio over a depth of 100 km and beneath which viscosity remains constant. Specifying the total anomalous mass for different sized anomalies, while keeping a similar viscosity structure means that we must specify the input viscosity independently from the input density and therefore cannot use a temperature-dependent viscosity. The input temperature field used when solving equation (19) is obtained by mapping our specified densities into "effective" temperature. We specify the viscosity input to CitcomT directly.

[36] While we have parameterized our input density in terms of temperature, this density can have either a compositional or thermal component. Since we are solving only for the instantaneous flow we do not need to distinguish between density anomalies arising from composition and those arising from temperature. This approach also has some additional benefits. In cratonic regions, lithospheric instability may only occur within the lower extent of the thermal boundary layer and be driven by compositional effects, perhaps due to phase changes [*O'Connell and Wasserburg*, 1972; *Kaus et al.*, 2005]. Compositional buoyancy may also be responsible for the apparent long-term stability of cratonic lithosphere [*Jordan*, 1978; *Kelly et al.*, 2003; *Sleep*, 2005]. Comparing our best fit input density models with density anomalies associated with different mineral phase changes may allows us to discern the relative roles of compositional and thermal density changes in cratons.

### 4.4. Results

[37] Preliminary modeling quickly showed that a half width of 600 km provided the best fit to observations, regardless of the viscosity structure, for anomalies contained within the upper mantle (we tested models ranging in half width from 100 to 800 km). This is most likely due to the large horizontal extent of the Congo gravity anomaly, along with our placement of the density anomaly within the upper mantle region. As a result, we only discuss model groups with 600 km half width here. The parameters of model groups we do discuss are given in Table 3 along with the depth, thickness, misfit and maximum density contrast associated with the best fit model of each group.

[38] The thickness and depth of the density anomalies controls their coupling to the surface as illustrated by the

**Figure 9.** Cross sections through the center of a sample input model with half width of 600 km, half depth of 100 km, depth of 100 km, $r = 1000$, $v_T = 4.35$, and total anomalous mass of $9 \times 10^{18}$ kg. (a) Input density structure. The maximum density anomaly is +27 kg m$^{-3}$. (b) Background viscosity structure. (c) Viscosity anomaly associated with the density anomaly in a). The value of the background viscosity structure at a depth of 50 km defines the maximum viscosity of the anomaly. (d) The total viscosity structure is defined as max($\eta_{\text{background}}$, $\eta_{\text{anomaly}}$). Defining the viscosity in this manner allows the anomalous mass to be viscously coupled to the lithosphere smoothly and without increasing the viscosity within the lithosphere.

**Table 3.** Summary of Model Groups

| Group Parameters | | | | | | Best Fit Model From Each Group | | | | | | |
|---|---|---|---|---|---|---|---|---|---|---|---|---|
| Group | $v_T$ | $\eta_{eqv}$ Depth (km) | Mass Anomaly ($10^{18}$ kg) | $Z_{lm}$ (km) | $r_{lm}$ | Model | Anomaly Depth (km) | Half Thickness (km) | Gravity Misfit | Topography Misfit | Total Misfit | $\Delta\rho_{max}$ (kg m$^{-3}$) |
| 1 | 4.35 | 0 | 9 | - | 1 | I806 | 100 | 50 | 0.398 | 0.686 | 0.542 | 54 |
| 2 | 4.35 | 50 | 8 | - | 1 | I790 | 100 | 100 | 0.395 | 0.681 | **0.538** | 27 |
| 3 | 4.35 | 50 | 9 | - | 1 | I546 | 100 | 100 | 0.381 | 0.682 | **0.532** | 30 |
| 4 | 4.35 | 50 | 10 | - | 1 | I506 | 100 | 50 | 0.378 | 0.695 | **0.537** | 60 |
| 5 | 4.35 | 50 | 14.7 | - | 1 | I763 | 50 | 50 | 0.376 | 0.900 | 0.638 | 100 |
| 6 | 4.35 | 100 | 9 | - | 1 | I832 | 100 | 100 | 0.385 | 0.682 | **0.534** | 30 |
| 7 | 0.1 | 50 | 8 | - | 1 | I895 | 100 | 100 | 0.387 | 0.680 | **0.534** | 27 |
| 8 | 0.1 | 50 | 9 | - | 1 | I848 | 100 | 50 | 0.381 | 0.684 | **0.533** | 54 |
| 9 | 0.1 | 50 | 10 | - | 1 | I530 | 100 | 50 | 0.387 | 0.699 | 0.543 | 60 |
| 10 | −0.9 | 50 | 10 | - | 1 | I489 | 50 | 50 | 0.401 | 0.702 | 0.552 | 68 |
| 11 | 10 | 50 | 9 | - | 1 | I874 | 100 | 100 | 0.383 | 0.682 | **0.533** | 30 |
| 12 | 4.35 | 50 | 6 | - | 1 | I924 | 200 | 50 | 0.386 | 0.714 | 0.550 | 36 |
| 13 | 4.35 | 50 | 14.7 | 500 | 50 | I718 | 300 | 50 | 0.409 | 0.689 | 0.549 | 93 |
| 14 | 4.35 | 50 | 14.7 | 400 | 20 | I742 | 300 | 50 | 0.419 | 0.704 | 0.561 | 93 |
| 15 | −0.9 | 50 | 9 | - | 1 | I944 | 100 | 50 | 0.389 | 0.686 | **0.538** | 54 |

trends in the magnitude of the topographic depression (Figure 11). For group 3 (Figure 11a), as the density anomalies are placed deeper, the resultant deflection of the surface decreases. Note that this occurs even as the anomalies get thicker because the total anomalous mass remains constant. Thicker anomalies, however, have larger deflections for a given depth than do thinner ones, resulting from the greater viscous coupling to the surface. This effect is reduced if the maximum viscosity of the anomalies decreases: the only difference between group 3 and group 6 in Figures 11a and 11c is $\eta_{eqv}$, which equals 50 km for group 3 and 100 km for group 6. Note, however, that for a given depth the topographic deflection within group 6 is relatively constant compared with the higher-viscosity anomalies of group 3. For anomalies with a 50 or 100 km half thickness, increasing the rate at which the background viscosity decays determines the magnitude of the decrease in topographic deflection (Figure 12). Model groups in which the anomalies have a viscosity similar to that of the uppermost lithosphere, or in which the viscosity decays more slowly with depth (groups 1 and 8; Figures 11b and 11d) exhibit increased topographic deflections with depth for a few cases (i.e., 100 km half thickness in Figure 11d and 200 km half thickness in Figure 11b). In addition, the models with the maximum topographic deflection within these groups have larger half widths. While these deflections are larger in magnitude, they are also narrower in width (Figure 13). Thus the thick high-viscosity region associated with these models focuses the distribution of stress on the surface to a narrower region.

[39] The symbol size in Figure 11 is proportional to the topographic misfit for each model (Appendix B). The topography, taken by itself, does not strongly constrain our models because while for the models in Figure 11, the topography is fit best by shallow models, increasing the total mass anomaly would shift the best fitting models deeper.

[40] The topographic component of the gravity follows the same trends outlined above for the topography; however, the addition of the gravity due to the density anomaly changes these trends somewhat when considering the total gravity anomaly (Figure 14). The gravity due to the density anomaly decays much faster, as density anomalies shift deeper, than does the topography. This is seen in Figure 14a where, for shallow depths, the gravity has a magnitude of −40 mGal. As the mass anomaly gets deeper, the positive gravity due to the mass anomaly decreases rapidly and therefore cannot counteract the large negative gravity anomaly caused by the topographic deflection. Thus for deep models in Figure 14a, the gravity is extremely negative (near −100 mGal). This effect is even stronger for models in which the density anomaly remains strongly coupled to the surface at greater depths (Figures 14b and 14d). For group 6 this effect is not as strong because of the reduced topographic deflection for the deeper models due to weak surface coupling. From Figure 11c it can be seen that the topographic depression for the deepest models in group 6 is less than the deepest models of the other groups in Figure 11. When the density anomaly is placed deep in the mantle, its influence on observed gravity is minimal; the observed gravity is that due to the surface deflection, which is smaller for group 6 than for the strongly coupled models.

[41] Another interesting effect seen in Figure 14 for models with 50 km half width is an increase in the goodness of model fit as the density anomaly gets deeper. This occurs because for the deeper models, the topography and its gravity anomaly are reduced because of reduced surface coupling. At the same time the magnitude of the gravity due to the density anomaly is also reduced because it is deeper in the mantle. Since the net gravity is the difference of these two magnitudes this difference matches observations better than if either quantity were larger. This is true in general, and it is possible to match the observed gravity well even when the topographic deflection is under or over predicted. An example is model I924, the best fitting model in group 12 (Table 3). This model fits the gravity well but the topography poorly. Thus, the gravity taken alone is not a sufficient constraint on the density and viscosity of our models.

[42] The gravity and topography taken together do provide a stronger constraint on the density and viscosity of our

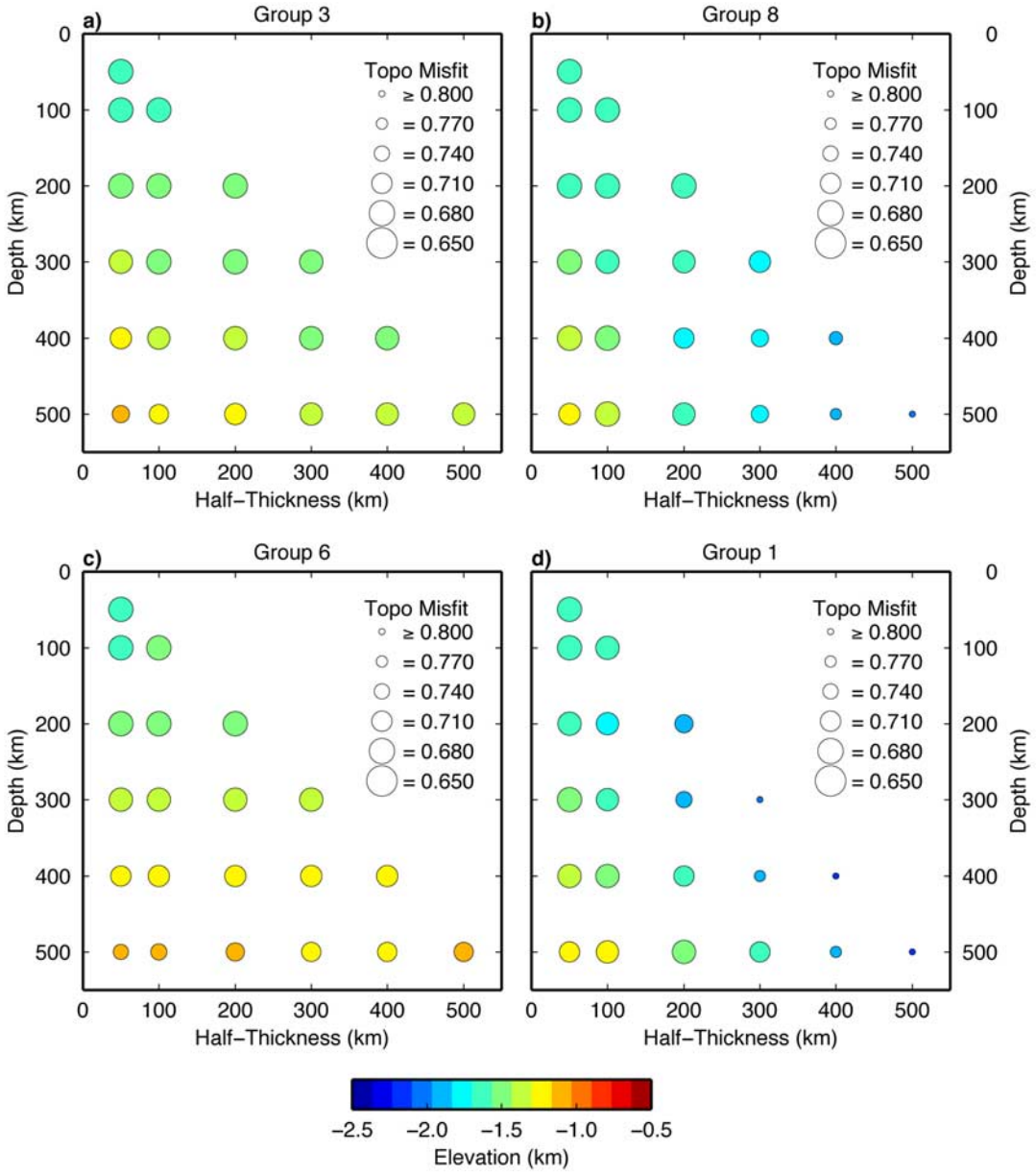


**Figure 11.** Model topography for several groups presented in Table 3. In all cases the total mass anomaly is $9 \times 10^{18}$ kg and the lower mantle is isoviscous. The symbol size indicates goodness of fit with observations with a larger symbol meaning a better fit (see Appendix B). The color of each symbol displays the maximum topographic depression observed at the center of the Congo basin. Other viscosity parameters are (a) group 3, $\eta_{eqv}$ depth of 50 km, $v_T = 4.35$. (b) Group 8, $\eta_{eqv}$ depth of 50 km, $v_T = 0.1$. (c) Group 6, $\eta_{eqv}$ depth of 100 km, $v_T = 4.35$. (d) Group 1, $\eta_{eqv}$ depth of 0 km, $v_T = 4.35$. See text for a detailed discussion of these models.

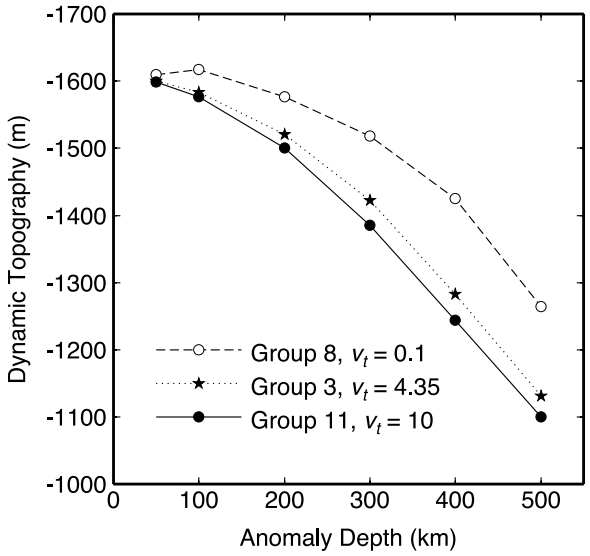


**Figure 12.** Magnitude of topographic deflection for models with different background viscosity profiles. All cases have the same mass anomaly of $9 \times 10^{18}$ kg and half thickness of 50 km. The topographic depression is nearly the same for all viscosity profiles at a depth of 50 km; however, the depression for models whose profile is superexponential ($v_T$ = 4.35 and 10) decays more quickly with depth than the models with a near exponential viscosity profile ($v_T$ = 0.1).

models. The topographic deflection is related to the anomalous density via the viscosity structure and determines the topographic component of the gravity. The total gravity is, in addition, also directly sensitive to the input density. The tradeoffs discussed above, associated with fitting either the topography or the gravity alone are therefore eliminated. This can be seen in the plots of model admittance and total model fit (Figures 15 and 16). Both these quantities are sensitive to topography and gravity. The best fit model admittances occur for models at 100 km depth. Models situated deeper in the mantle have a very large gravity anomaly compared to the topographic deflection and therefore admittances are large. Conversely, anomalies at a shallower depth have a subdued gravity due to the increasing gravitational influence of the anomalous mass compared to that of the topography (in the limit of a density anomaly at the surface the total gravity goes to zero). The total misfit shows a similar pattern to the admittance with best fitting models corresponding to a density anomaly at 100 km depth. The overall best fitting model is in group 3, located at 100 km depth and with a 100 km half thickness (Table 3). The best fitting models for all groups (except group 12 as discussed above) with an isoviscous lower mantle are located at 50 or 100 km depth with most occurring at 100 km. These best fitting models are also relatively thin with half thicknesses of either 50 or 100 km. The overall best fitting model, I546 in group 3, matches the observed gravity, topography and admittance well: The residual gravity and topography anomalies are small and the anomalous gravity, topography and admittance spectra are well reproduced (Figures 17, 18, and 19). The other models in Table 3 whose total misfit is less than about 0.540 fit similarly well.

[43] Our best fitting models provide a better constraint on the density structure than on the viscosity structure. The total anomalous mass of the best fitting models in Table 3 ranges only from 8 to $10 \times 10^{18}$ kg. Since these anomalies are constrained to be relatively thin and contained within the lithosphere, this corresponds to a maximum anomalous density range of 27–60 kg m$^{-3}$. Increasing or decreasing the anomalous mass outside this range results in models which fit the data poorly. It is possible to achieve a better fit for larger anomalous masses by providing some support to the anomalies by introducing a viscosity increase for the lower mantle. Groups 5 and 13 have the same total anomalous mass; however, the best fitting model in group 13 is situated 300 km deep, beneath the lithosphere and in a

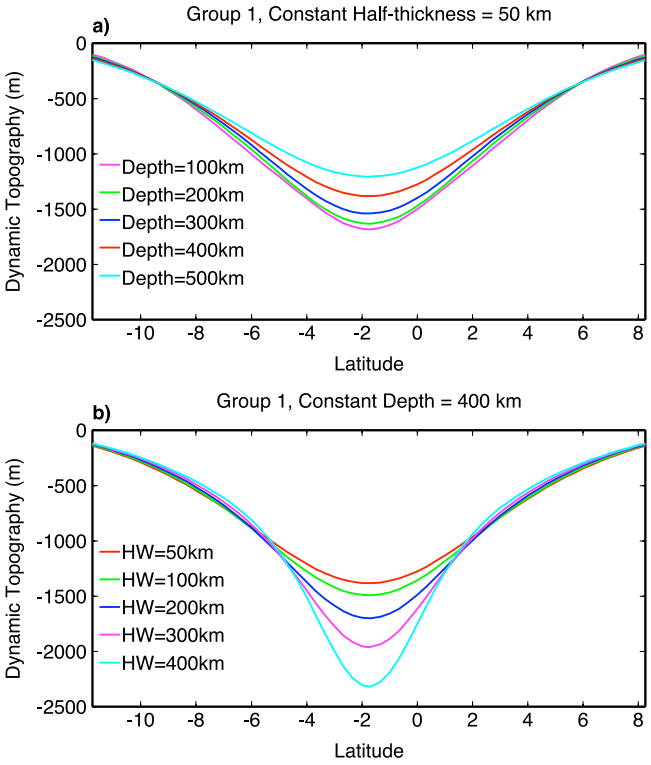


**Figure 13.** Profiles of model topography along a north-south transect through the Congo basin at 22°E. The profiles here are for models in group 1. These models all have a relatively high viscosity associated with the density anomaly. (a) Group 1 models whose half thickness is 50 km for various depths (the model at 50 km depth has been left out for clarity: it is very similar to the profile for the model at 100 km depth). The magnitude of the depression for these models decreases as the anomaly gets deeper, while the width remains relatively constant. (b) Group 1 models whose depth is 400 km. Thicker anomalies are more strongly coupled to the surface so the magnitude of the depression for these models increases with anomaly thickness. Note, however, that there is also a significant narrowing of the depression for the models whose anomaly is thickest. The red curve in Figures 13a and 13b are for the same model and provides a reference shape.

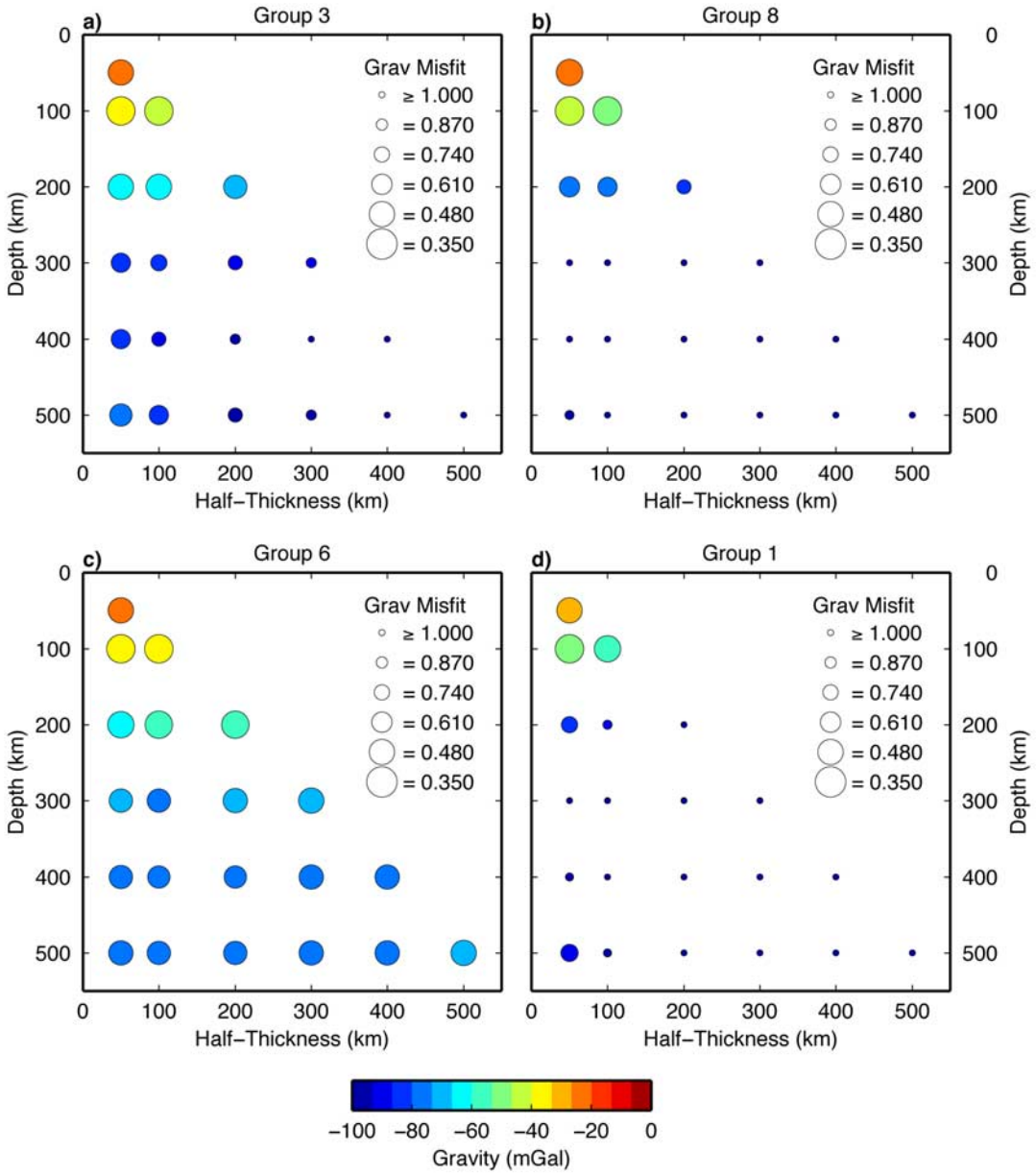


**Figure 14.** Same as Figure 11, except symbol size represents gravity misfit and symbol color represents total gravity anomaly at the center of the Congo basin.

location where some of the mass is supported by the higher viscosity transition zone and lower mantle. In contrast, the best fitting model of group 5 is located at 50 km depth, but fits much more poorly. An increase in viscosity beneath the lithosphere, however, has little effect on the fit of the anomalies situated within the lithosphere: The 50 km thick 50 km deep density anomaly in group 13 fits the data about as well as that of group 5 with a total misfit of 0.633 versus 0.638. We cannot uniquely determine the magnitude of the viscosity increase from the upper to lower mantle because there is a tradeoff between the depth of the viscosity increase and the magnitude of that increase (Compare groups 13 and 14 in Table 3). From Table 3 it can be seen, however, that these deeper models supported by a high-viscosity lower mantle fit the gravity much less well than the best fitting models with density anomalies located at shallower depths for groups with less total mass. This poor fit results from the upward continuation of the gravity due to the density anomaly. For these deep density anomalies, a large mass is required to fit the topography adequately; however, upward continuation of the gravity due to the mass anomaly shifts its spectral content out of the band containing the anomalous Congo basin gravity by preferentially damping shorter wavelengths. This effect can be counteracted by decreasing the width of the anomaly, in effect making the gravity shorter wavelength before upward continuation; however, doing so results in a poorer fit to the topography, which is not affected by the spectral dampening related to upward continuation. Thus the near coincidence of the spectral content of the anomalous topography and the

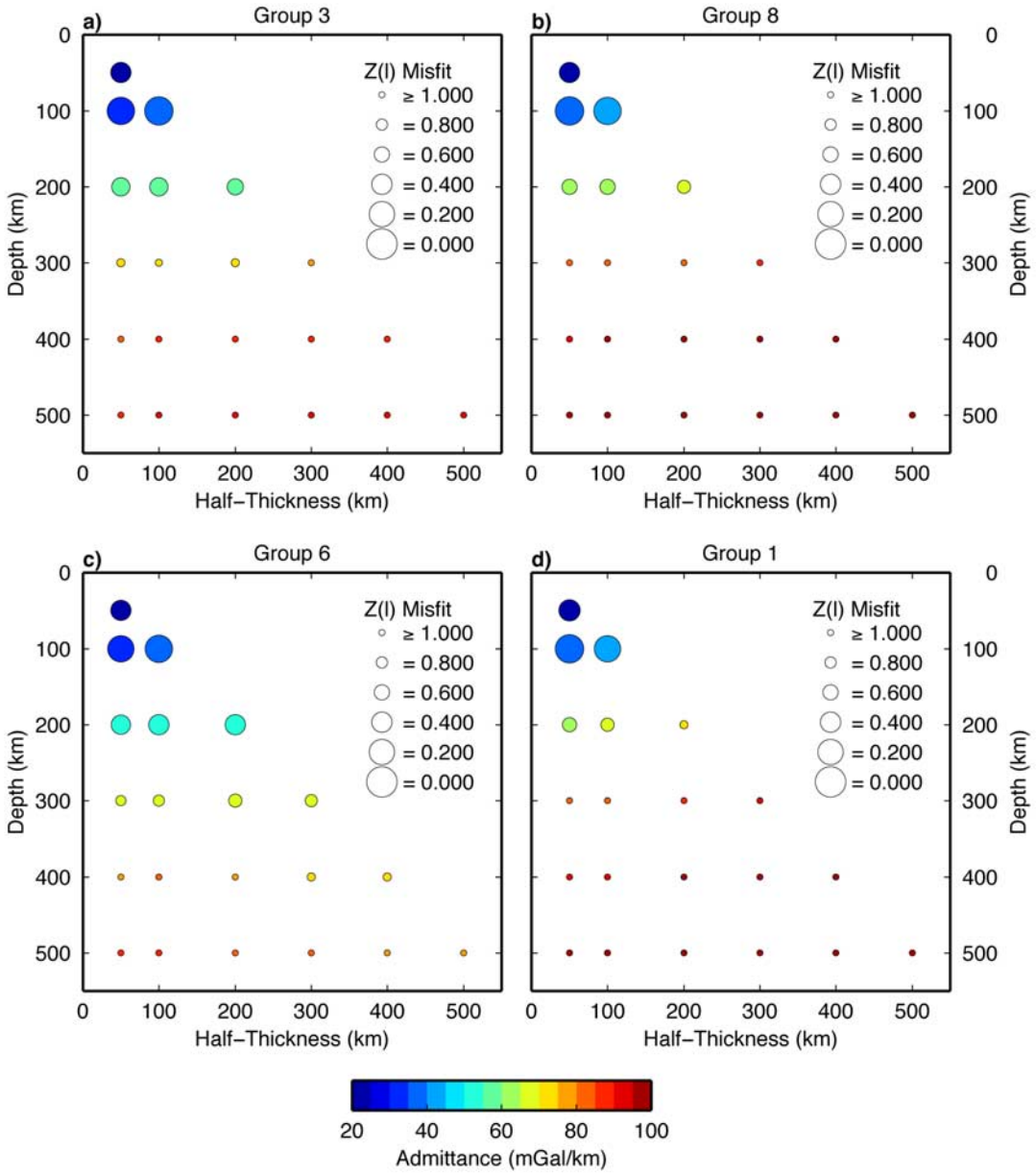


**Figure 15.** Same as Figure 11, except symbol size represents admittance misfit and symbol color represents average admittance observed over the band $20 < l < 40$ when gravity and topography are localized near the center of the Congo basin.

anomalous gravity implies a shallow source of the mass anomaly resulting in topographic deflection.

[44] Unfortunately, we are not able to constrain the viscosity structure of the lithosphere with our models. The three best fitting individual models in Table 3 have the same mass anomaly with the same maximum viscosity but have significantly different background viscosity profiles. Furthermore, we can also achieve a good fit using a model in which the maximum viscosity of the anomaly is significantly less than the maximum viscosity anomaly of our overall best fit model. This inability to constrain the viscosity structure within the lithosphere probably results from the shallow location of the density anomaly. At these depths there is no significant difference in the strength of coupling between the anomaly and the surface for different viscosity structures. As a result, these various viscosity structures result in a similar topographic depression at the surface for shallow density anomalies (Figure 11).

### 4.5. Calculation of Synthetic Tomographic Images

[45] In addition to our dynamic solutions we also create synthetic tomographic images for our various input models. We utilize the filtering procedure of *Ritsema et al.* [2007] to obtain the images expected for our input model geometries, assuming resolution characteristics consistent with S20RTS (Figure 20). Previous authors have used either empirical calibration of shear wave velocity and temperature [e.g., *Priestly and McKenzie*, 2006] or have relied on mineral physics constraints to scale temperature perturbations into

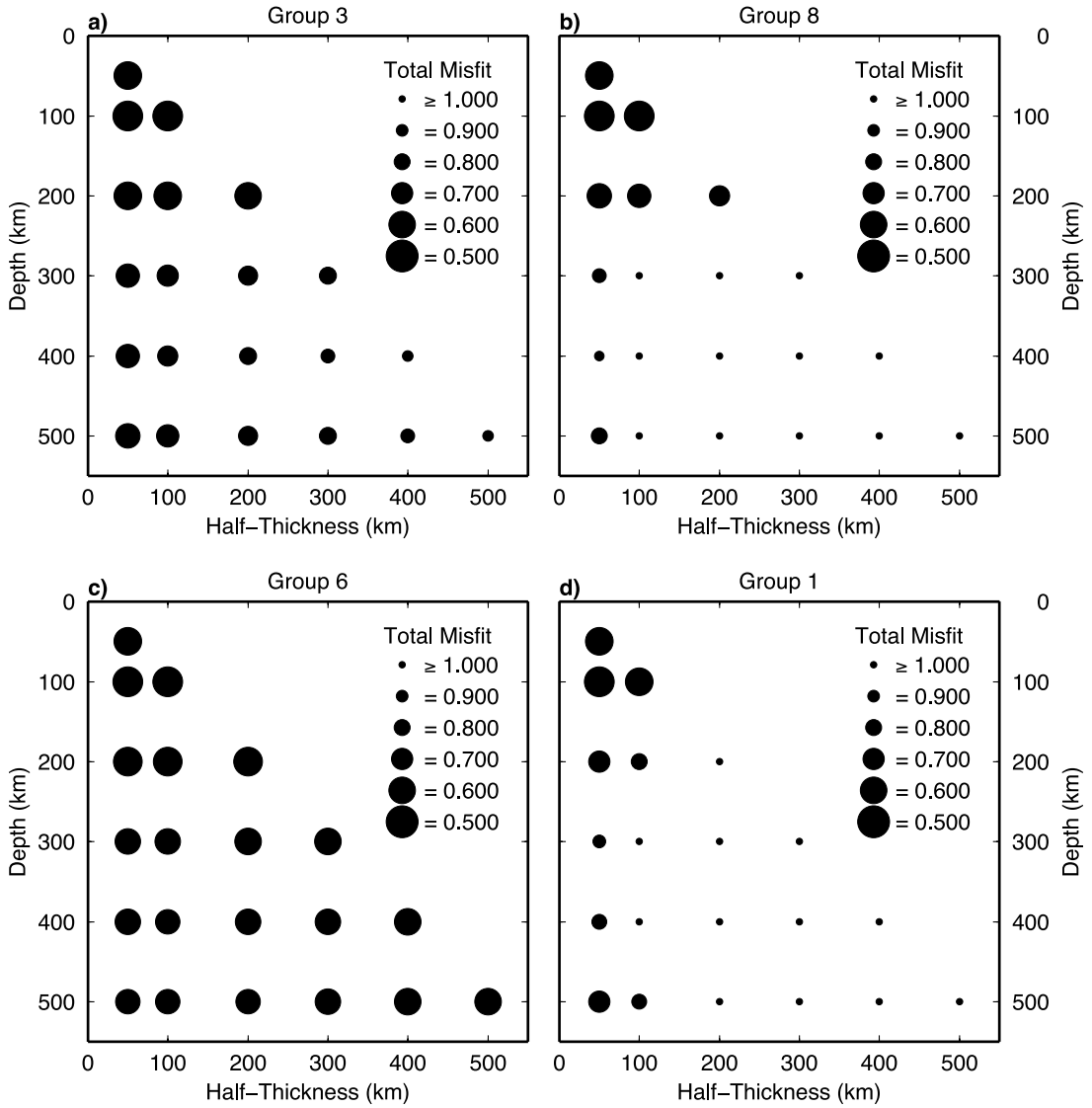


**Figure 16.** Same as Figure 11, except symbol size represents total misfit.

velocity perturbations [e.g., *Tan and Gurnis*, 2007]. However, we assume that the shear wave velocity anomaly resulting from our models follows the same bivariate Gaussian pattern and has unit amplitude. This approach avoids the need to scale geodynamic variables by poorly determined conversion factors [see *Karato*, 2008]. In order to quantify the fit between the synthetic images and those of S20RTS, we derive a misfit parameter based on the correlation coefficient which is localized horizontally using the same spatiospectral localization used for the gravity and topography, and localized to the upper mantle using a combination of the S20RTS basis splines (see Appendix B).

[46] The local correlations observed for the various input models ranges from 0.28 to 0.47 (Figure 21). At the long wavelengths associated with S20RTS (we are restricted to $l < 20$, which for $f_s = 1.5$ yields $L_{Nyq} = 12$), our windowing functions include a large area surrounding the Congo basin where our models are not defined, resulting in the overall low correlation values in Figure 17. However, these correlation values still provide a relative measure of model fit. The greatest variation in correlation occurs for models with a 50 km half width, with the overall best and worst fitting models occurring at 100 and 200 km, respectively. That these models occur at adjacent depths is indicative of the rapid change with depth in shear wave velocity anomaly that occurs in the uppermost regions of S20RTS beneath the Congo (Figure 7). At 100 km half thickness the depth variation of correlation is decreased; however, the best fit model still occurs at 200 km depth. For half thicknesses greater than or equal to 200 km, all models fit the observations equally well. This lack of variation results from the relatively constant shear wave velocity anomaly of S20RTS over these larger depth ranges within the upper 800 km of the mantle beneath the Congo basin.

## 5. Discussion and Conclusions

[47] The observations outlined in section 3 demonstrate that the Congo basin's surface is currently being depressed in response to the downward flow of an anomalously dense region in the mantle. This geodynamic scenario is similar to that generically proposed by *DeRito et al.* [1983] and

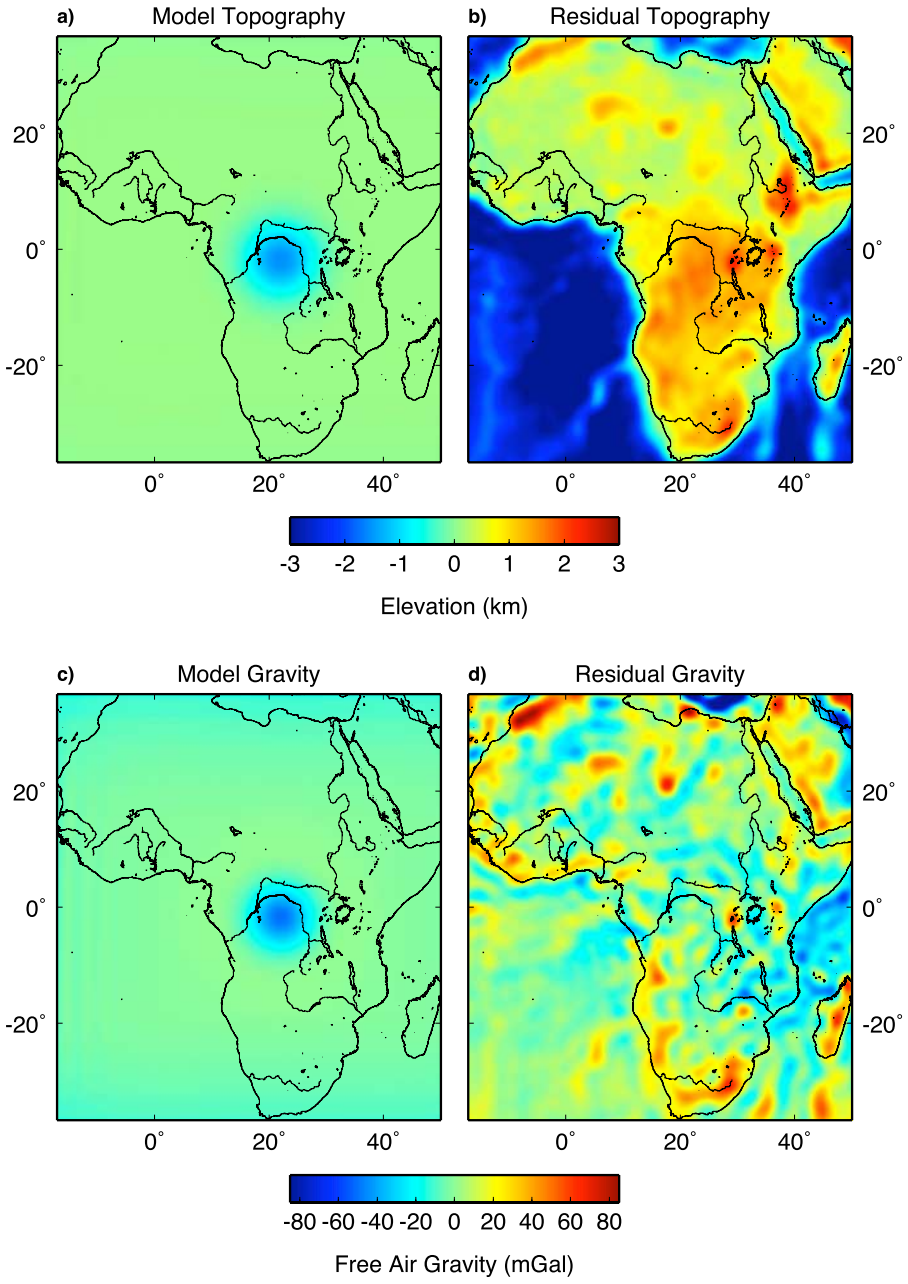


**Figure 17.** Sample model output for our overall best fitting model (model I546; Table 3). (a) Model topography reaches maximum amplitude of about 1.4 km near the center of the Congo basin. (b) Residual topography calculated by subtracting the model in Figure 17a from the sediment-corrected topography displayed in Figure 4b. The absence of any significant depression at the location of the Congo basin demonstrates the very good fit to observations we are able to achieve with our dynamic models. (c) Model gravity for our best fit model. This model gravity reaches −70 mGal minimum magnitude at the center of the Congo basin. (d) Residual gravity given by subtracting the model gravity from the GRACE gravity shown in Figure 2a. Again, there is no systematic misfit observed in the Congo region indicating a good fit. Overall, we are able to fit the gravity and topography of the Congo basin using several models whose output is similar to those described here (see Table 3).

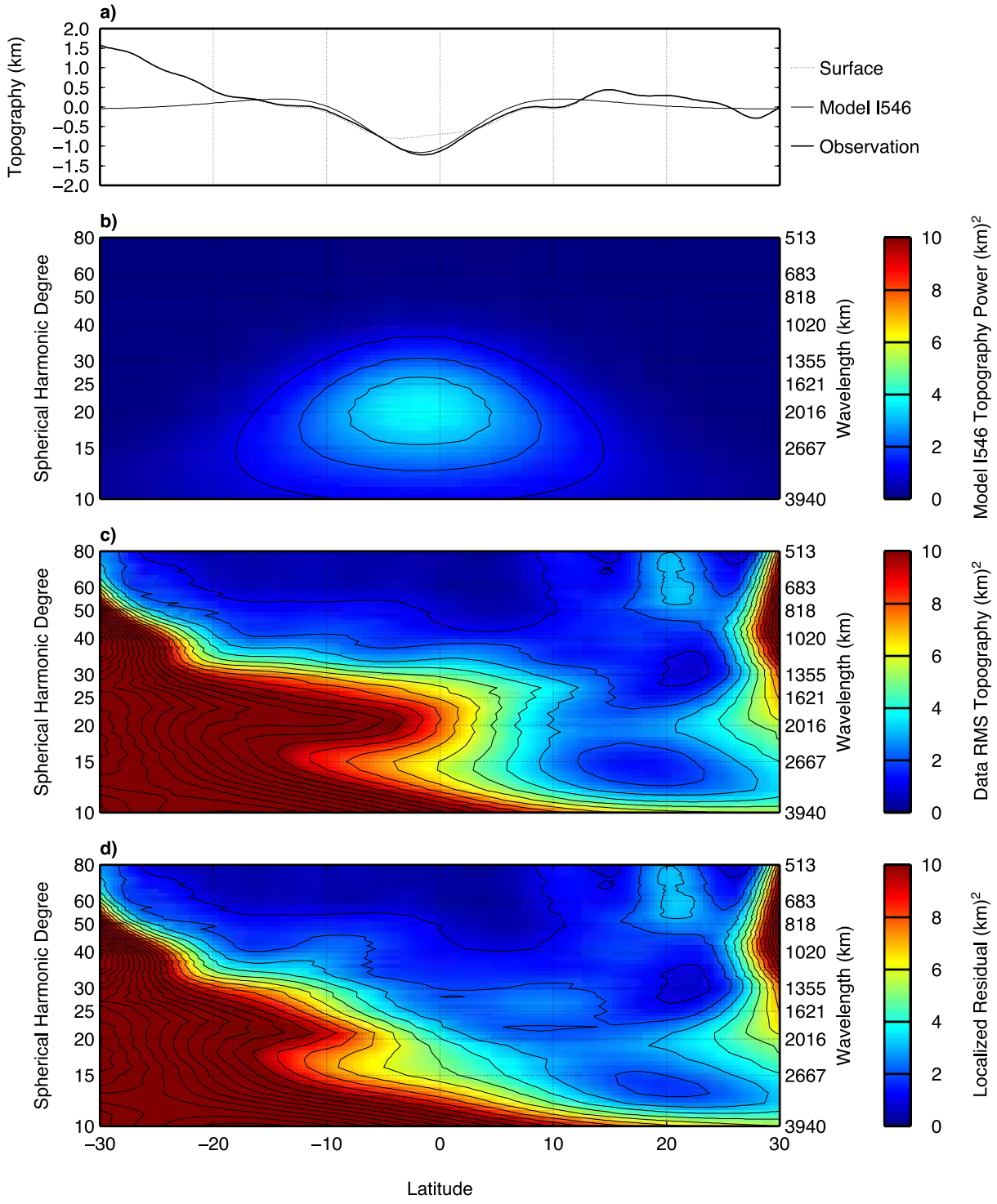


**Figure 18.** (a) Band-passed topographic profile of our best fit model, I546, along with the sediment unloaded topography (“observation”) and the original SRTM topography (“surface”) at longitude 22°E. The model fits the data the best near the center of the Congo basin. The large southward increase in the observed topography south of the basin is due to the high elevations of southern Africa. (b) Model power “spectrogram” along the profile in Figure 18a. Each vertical slice of this image represents the power spectrum of the model in Figure 18a localized near the latitudes along the profile. Note that the model power is localized near the Congo basin. (c) Spectrogram of the “observation” profile in Figure 18a. Note the anomalous RMS topography near the Congo, superimposed upon a triangular-shaped region of high topography power in southern Africa. (d) Localized residual sum of squares (RSS) for model I546 (see Appendix B). The localized RSS is equivalent to the data power minus the model power, so it is equal to the image in Figure 18c minus the image in Figure 18b. Note that much of the anomalous power associated with the Congo basin has been removed.

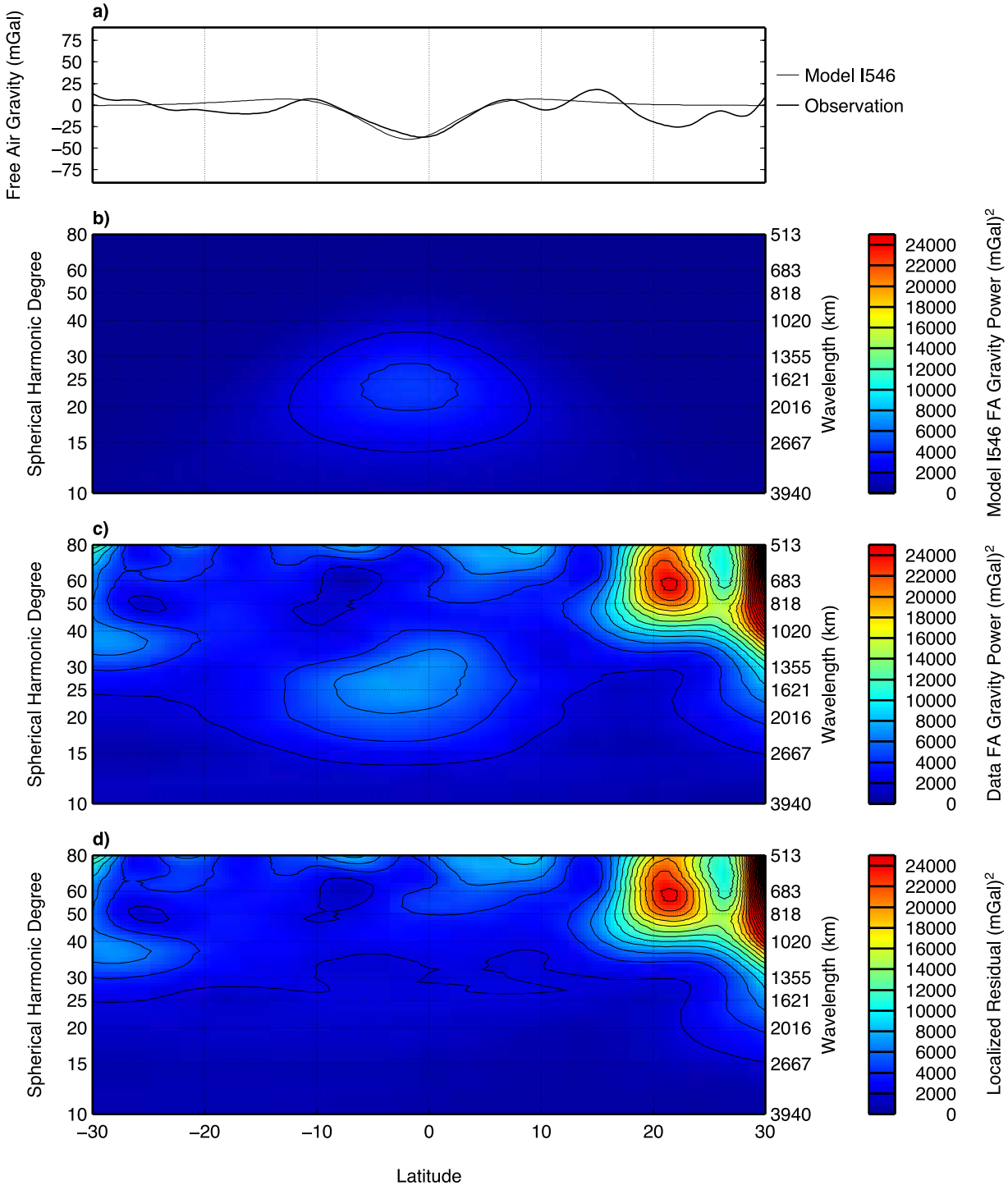


**Figure 19.** Same as Figure 18, but for gravity. Note that in Figure 19c the Congo gravity anomaly is isolated from other anomalies. In Figure 19d much of the anomalous power of gravity has been removed indicating a good model fit at the Congo basin and over the wave band containing the Congo gravity anomaly.

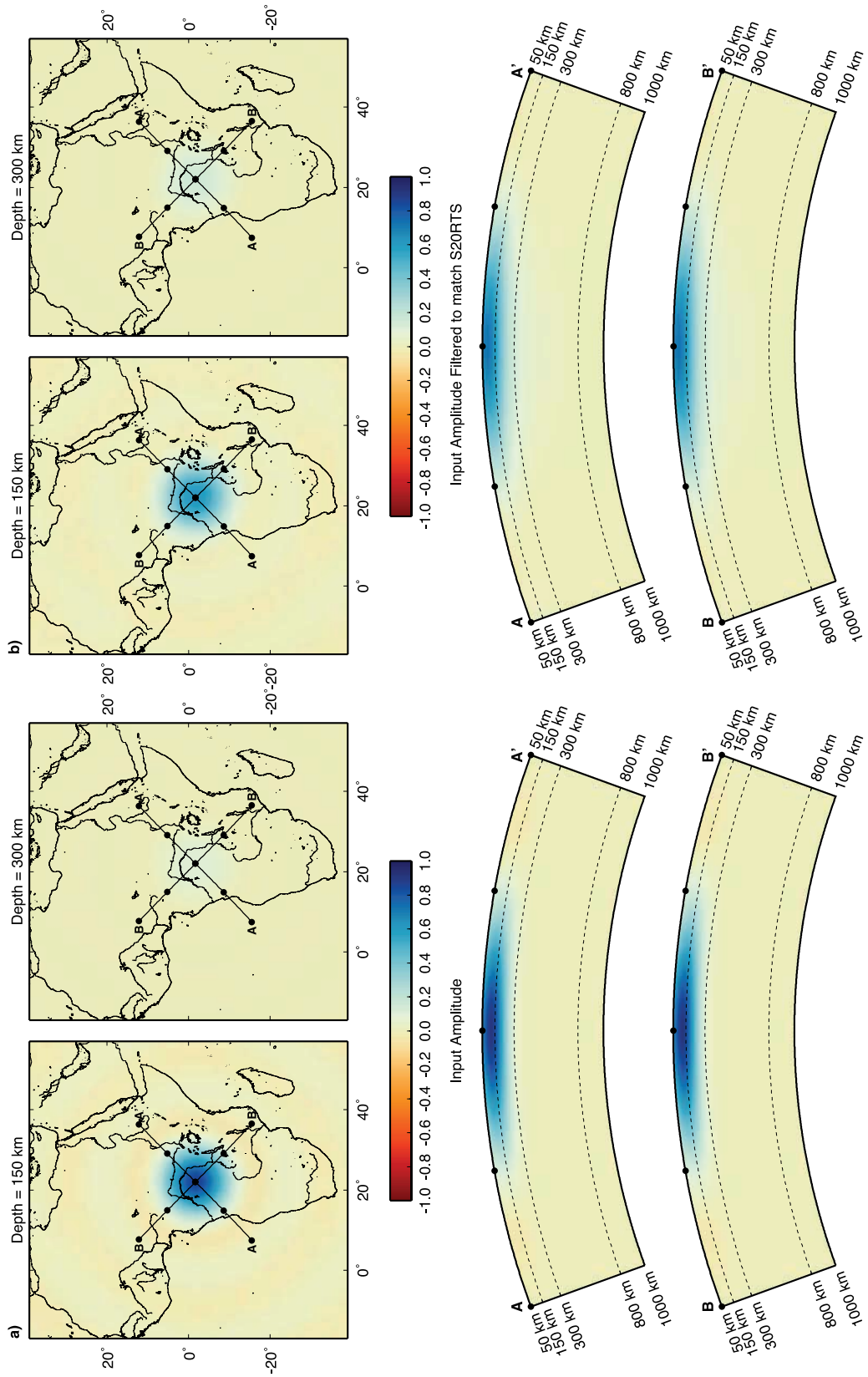


**Figure 20.** (a) Same as Figure 7 for the input seismic velocity anomaly for a 100 km deep, 100 km wide anomaly of unit amplitude. This model has been projected onto the S20RTS tomography model's basis. (b) Output of the filtering process of *Ritsema et al.* [2007] for the input model in Figure 20a. The presence of this anomaly in the upper mantle is consistent with the observations in Figure 7.

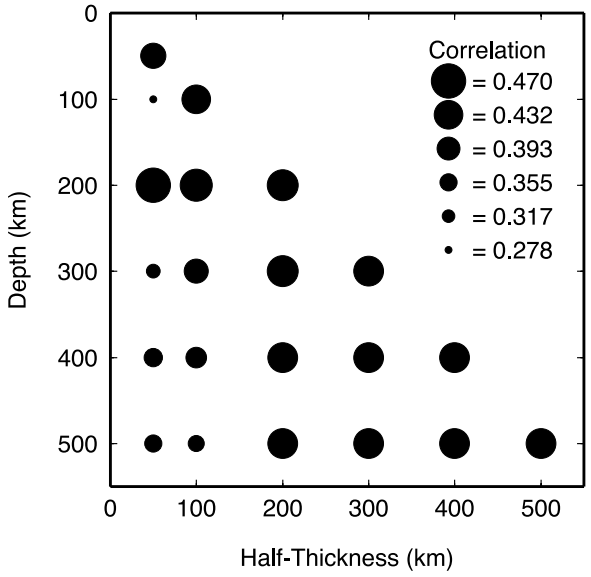


**Figure 21.** Localized correlation coefficients between modeled and observed shear wave velocity anomalies for the model geometries used here. Larger symbols indicate better fit. These coefficients have been calculated by localizing the correlation between the model and S20RTS basis splines to the uppermost mantle and horizontally to the Congo region using spatiospectral localization.

*Naimark and Ismail-Zadeh* [1995] in which density anomalies like the one described here periodically become unstable and cause subsidence of intracratonic basins. While our observations do not indicate what stage of the subsidence process the Congo basin is currently undergoing, they do provide the best evidence thus far that intracratonic basin subsidence is driven by dynamic topography and that the most recent depression of the Congo basin is dynamically maintained. Models in which anomalous masses within the cratonic lithosphere become unstable in response to global tectonic events are also the most plausible mechanism to explain the long-period near synchronicity of intracratonic basin subsidence worldwide [*Sloss*, 1990].

[48] The gravity and topographic anomalies associated with the Congo basin also provide constraints on the density structure of the lithosphere. Simultaneously fitting both gravity and topography allow us to determine the magnitude of the total mass anomaly associated with the Congo anomaly. We are also able to constrain this anomaly as being located within the lithosphere at a depth of 100 km. The maximum density contrast across this anomaly ranges from 27 to 60 kg $m^{-3}$, depending on its half width and thickness. If the density anomaly has a thermal origin this corresponds to a temperature drop of about 400–900 K, relative to ambient mantle, assuming a thermal expansivity, $\alpha$, of $2 \times 10^{-5}$ $K^{-1}$. Such a large temperature anomaly implies that the lithosphere beneath the Congo basin has a temperature similar to that of the crust. Correspondingly, the viscosity of such a cold mantle region should be large [*Priestly and McKenzie*, 2006]. Our modeling results do show, however, that even for a linear viscosity profile through the lithosphere the observations are not fit well. It is much more likely that the origin of these large density anomalies is largely compositional. Density changes associated with the eclogite phase transition can easily explain the observed density contrasts without requiring the presence of a large thermal anomaly and associated high viscosities beneath the Congo basin [*Anderson*, 2007a].

[49] We are not able to tightly constrain the viscosity of the lithosphere beneath the Congo basin. This inability arises from the location of the preferred anomaly in the uppermost mantle where it is tightly coupled to the surface for a range of viscosity structures, including exponential and two superexponential decay rates. It does appear that a linear viscosity profile through the lithosphere is inconsistent with observations. Thus we are unable to determine the exact nature of the decrease in lithospheric viscosity with depth.

[50] The density and viscosity structure of the lithosphere determined from gravity and topography is consistent with the shear wave velocity anomaly observed beneath the Congo basin. However, the exact placement of that anomaly appears deeper in the lithosphere than our preferred models. This difference in location may result from an offset of the location of the center of the density anomaly and the location of maximum seismic velocity anomaly. For example, a region of constant seismic velocity with depth will have a greater velocity anomaly at greater depths relative to PREM due to the increase in background velocity within PREM. In this analysis we have ignored the amplitude of the seismic velocity anomalies when comparing various models and the resolution of S20RTS limits us to very large scales. Perhaps a more detailed analysis and a higher resolution model will provide more constraints on the structure of the Congo lithosphere. Another implication for the tomographic analysis is the influence of composition on seismic velocity. *Anderson* [2007b] shows that for eclogitic bodies within the uppermost mantle, density and seismic velocity are not strongly correlated. Indeed it is possible to have a high-density region which is not observed seismically. If this is indeed the case beneath the Congo basin, and the density anomaly is caused by an eclogite phase transition, this may explain the lack of lithospheric root beneath the Congo basin observed in the tomographic model of *Pasyanos and Nyblade* [2007].

[51] In conclusion, the observations of topography and gravity at the Congo basin indicate a dynamic origin for the depression of the basin's surface. These observations taken together indicate that the density anomaly causing this subsidence is located within the upper mantle at a depth of 100 km. In addition the magnitude of this density anomaly is 27–60 kg $m^{-3}$, a range most consistent with a compositional origin. We are not able to constrain the exact nature of the viscosity structure of the lithosphere. It does appear, however, that the decay of viscosity with depth is exponential or superexponential. While we cannot claim our models fit the data uniquely, because of the nonlinear nature of mantle convection, it does appear that our best fitting models are the most reasonable assuming realistic lithospheric density and viscosity structures.

## Appendix A: Definition of Admittance

[52] Admittance analyses attempt to estimate the linear transfer function between topography and gravity. The most

general linear transfer function between two functions, $A$ and $B$ defined on the surface of the sphere, $\Omega$, is given by

$$B(\hat{u}) = \int_{\Omega} F(\hat{u}, \hat{v}) A(\hat{v}) d\Omega. \tag{A1}$$

[53] The hat ($\hat{}$) symbol is used to denote unit vectors pointing from the center of the sphere to a location ($\theta$, $\phi$) on the sphere's surface. Generally the transfer function between topography and gravity is assumed to be isotropic (see *McNutt* [1979] for an exception). Physically, this means that there is no azimuthal bias about the point $\hat{u}$ in the transfer function $F$, or equivalently, that $B(\hat{u})$ is only dependent on the zonal components of $A(\hat{v})$ about the pole $\hat{u}$. It is also generally assumed that the transfer function is spatially invariant on the surface of the sphere. Mathematically, these two assumptions mean that $F$ has no explicit dependence on the location $\hat{u}$ depending only on the angular separation between the points $\hat{u}$ and $\hat{v}$, i.e., that $F(\hat{u}, \hat{v}) = F(\hat{u} \cdot \hat{v})$. Substituting this relation into equation (A1) gives a convolution integral [*Basri and Jacobs*, 2003]. These convolution integrals are most conveniently expressed in the spherical harmonic domain.

[54] We adopt the *Varshalovich et al.* [1988] normalization for the spherical harmonic functions:

$$Y_{lm}(\theta, \phi) = (-\mathrm{sgn}(m))^m \sqrt{\frac{(2l+1)}{4\pi} \frac{(l-|m|)!}{(l+|m|)!}} P_{l|m|}(\cos\theta) e^{im\phi}, \tag{A2}$$

$l = 0, 1, 2, \ldots$ and $m$ is an integer such that $-l \leq m \leq l$. $P_{lm}$ are the associated Legendre functions, defined for $m \geq 0$ as

$$\begin{aligned} P_{lm}(\cos\theta) &= (\sin\theta)^m \frac{d^m}{d(\cos\theta)^m} P_l(\cos\theta) \\ &= (-1)^l \frac{(\sin\theta)^m}{2^l l!} \frac{d^{l+m}}{(d\cos\theta)^{l+m}} (\sin\theta)^{2l}, \end{aligned} \tag{A3}$$

where $P_l$ are Legendre polynomials. These spherical harmonic functions are normalized such that

$$\int Y_{lm}(\theta, \phi) Y^*_{l'm'}(\theta, \phi) d\Omega = \delta_{ll'} \delta_{mm'}. \tag{A4}$$

[55] Continuous functions on the sphere can then be represented by

$$A(\hat{v}) = A(\theta, \phi) = \sum_{l=0}^{\infty} \sum_{m=-l}^{l} a_{lm} Y_{lm}(\theta, \phi). \tag{A5}$$

The spherical harmonic coefficients $a_{lm}$ of the function $A(\theta, \phi)$ are given by

$$a_{lm} = \int_{\Omega} A(\theta, \phi) Y^*_{lm}(\theta, \phi) d\Omega. \tag{A6}$$

The cross power spectrum between two sets of spherical harmonic coefficients is defined as

$$S_{ab}(l) = \sum_{m=-l}^{l} a_{lm} b^*_{lm}. \tag{A7}$$

$S_{aa}(l)$ is termed the power spectrum. The correlation spectrum between two sets of coefficients is defined as

$$r(l) = \frac{S_{ab}(l)}{\sqrt{S_{aa}(l) S_{bb}(l)}}. \tag{A8}$$

Returning to the transfer function (A1), If we choose $\hat{u}$ as the $\theta = 0$ axis, then since $F$ only depends on $\theta$ we have the following spherical harmonic representation of the transfer function:

$$\begin{aligned} F(\hat{u}, \hat{v}) = F(\hat{u} \cdot \hat{v}) = F(\cos\theta) &= \sum_{l=0}^{\infty} \sqrt{\frac{4\pi}{2l+1}} F_l Y_{l0} \\ &= \sum_{l=0}^{\infty} F_l P_l(\cos\theta). \end{aligned} \tag{A9}$$

We can now transform equation (A1) using the Funk-Hecke theorem [*Basri and Jacobs*, 2003]:

$$B(\theta, \phi) = B(\hat{u}) = \int_{\Omega} F(\hat{u} \cdot \hat{v}) A(\hat{v}) d\Omega = \sum_{l=0}^{\infty} F_l \sum_{m=-l}^{l} a_{lm} Y_{lm}(\theta, \phi). \tag{A10}$$

Thus using (A5), replacing $A$ with $B$ and $a_{lm}$ with $b_{lm}$,

$$b_{lm} = F_l a_{lm}. \tag{A11}$$

Our goal is to estimate $F_l$ when $b_{lm}$ and $a_{lm}$ are the spherical harmonic coefficients of the gravity and topography, respectively. In general, equation (A11) will not hold for observed gravity and topography due to the presence of "noise" in the gravity. We need to modify equation (A11) to take this into account:

$$g_{lm} = F_l h_{lm} + n_{lm}, \tag{A12}$$

where $g_{lm}$ and $h_{lm}$ are the spherical harmonic coefficients of gravity and topography and $n_{lm}$ are the coefficients of the "noise." The "noise" in equation (A12) is defined as the component of the gravity which is uncorrelated with the topography, i.e., the cross power spectrum between the topography and the noise given by equation (A7) is zero for all $l$. Sources of this noise are not just measurement errors but also include any component of the gravity that cannot be linearly related to the topography. Defining the noise in this way allows us to calculate an estimate of $F_l$, denoted as $Z(l)$, by multiplying equation (A12) by $h^*_{lm}$ and summing over $m$ yields

$$Z(l) \equiv \frac{S_{gh}(l)}{S_{hh}(l)} = \frac{\sum_{m=-l}^{l} g_{lm} h^*_{lm}}{\sum_{m=-l}^{l} h_{lm} h^*_{lm}}, \tag{A13}$$

where $g_{lm}$ and $h_{lm}$ are the spherical harmonic coefficients of gravity and topography, respectively. $Z(l)$ is an unbiased estimate of the transfer function's spectrum [*Wieczorek*, 2007].

[56] If our assumption of a spatially invariant $F_l$ is violated, then $Z(l)$ estimates a globally averaged transfer function. However, we can examine the spatial variance in $F_l$ using spatiospectral localization. We denote the spherical harmonic coefficients of gravity and topography windowed near a point ($\theta_o$, $\phi_o$) by $\gamma_{lm}(\theta_o, \phi_o)$ and $\psi_{lm}(\theta_o, \phi_o)$ respectively. Substitution of these windowed coefficients into equation (6) gives a local estimate of $F_l$:

$$Z(l, \theta_o, \phi_o) = \frac{S_{\gamma\psi}(l, \theta_o, \phi_o)}{S_{\psi\psi}(l, \theta_o, \phi_o)}. \tag{A14}$$

Equation (7) assumes that $F$ is spatially invariant within a window. By centering these windowing functions at different locations we can explore the spatial variance of the transfer function.

## Appendix B: Calculation of Model Misfit

### B1. Tomography, Gravity, and Total Misfit

[57] The model misfit parameters used to determine which gravity and topography models best fit observations are based upon a localized version of the residual sum of squares (RSS):

$$\mathrm{RSS}(\Omega) = \frac{1}{4\pi} \int_{\Omega_o} (d(\Omega_o, \Omega) - m(\Omega_o, \Omega))^2 d\Omega_o, \tag{B1}$$

where $d(\Omega_o, \Omega)$ and $m(\Omega_o, \Omega)$ are the data and the model, respectively, localized near the location $\Omega$ using the spatiospectral localization method outlined in the text, and defined over the surface of the Earth $\Omega_o$. Using Parseval's theorem [*Wieczorek*, 2007], (B1) is transformed to

$$\mathrm{RSS}(\Omega) = \sum_{l=0}^{\infty} \sum_{m=-l}^{l} (D_{lm}(\Omega) - M_{lm}(\Omega))^2. \tag{B2}$$

In terms of the total cross power between two functions,

$$P_{AB} = \sum_{l=0}^{\infty} \sum_{m=l}^{-l} a_{lm} b_{lm}. \tag{B3}$$

Equation (B2) becomes

$$\mathrm{RSS}(\Omega) = P_{DD}(\Omega) + P_{MM}(\Omega) - 2P_{DM}(\Omega). \tag{B4}$$

Thus, the local residual sum of squares equals the power in the localized data plus the power in the localized model minus twice their cross power. In practice, the sum over $l$ in equation (B3) must be restricted to a finite range of $l$. We choose to sum the power over the wave band containing the anomalous topography and gravity, namely, $10 \leq l \leq 40$, when calculating the model misfit parameters. In order to combine the gravity and topography misfit we normalize (B4) by the localized data power, since the model power varies between models, but the data power does not:

$$\mathrm{RSSN}(\Omega) = \frac{\mathrm{RSS}(\Omega)}{P_{DD}(\Omega)} = 1 + \frac{P_{MM}(\Omega)}{P_{DD}(\Omega)} - 2\frac{P_{DM}(\Omega)}{P_{DD}(\Omega)}. \tag{B5}$$

RSSN($\Omega$) will equal 1 for the "null" model, $m(\Omega_o, \Omega) = 0$, and will equal 0 when the data and model match perfectly over our wave band of interest. Combining the gravity and topography normalized misfits is accomplished by averaging

$$\mathrm{RSSN}(\Omega)_{\mathrm{Total}} = \frac{1}{2}\left(\mathrm{RSSN}(\Omega)_{\mathrm{Topo}} + \mathrm{RSSN}(\Omega)_{\mathrm{Grav}}\right). \tag{B6}$$

Throughout this paper we use equations (B5) and (B6) to calculate model misfit when the data and model are localized near the center of the Congo basin at $\Omega$ = (22.00°Å, 1.75°S).

[58] A similar process is used to calculate the misfit of the localized admittance (A14). This misfit is based upon the root-mean-square residual of model and observed admittance over a specified wave band:

$$R_A(\Omega) = \sqrt{\frac{\sum_{l=l_{\min}}^{l=l_{\max}} (Z_o(l, \Omega) - Z_m(l, \Omega))^2}{l_{\max} - l_{\min}}}. \tag{B7}$$

We restrict the sum in equation (B7) to the wave band $20 \leq l \leq 40$ over which the observed admittance is anomalously high. We also normalize (B7) by the residual for the "null" model giving

$$RN_A(\Omega) = \sqrt{\frac{\sum_{l=l_{\min}}^{l=l_{\max}} (Z_o(l, \Omega) - Z_m(l, \Omega))^2}{\sum_{l=l_{\min}}^{l=l_{\max}} (Z_o(l, \Omega))^2}}. \tag{B8}$$

The admittance misfit is only used to identify which models give admittance values similar to those observed and is not included in the total misfit calculation since it is not an independent measure of model misfit.

### B2. Tomography Misfit

[59] S20RTS is parameterized in terms of spherical harmonic functions and 21 radial basis splines, defined on the domain $R_{CMB} < r < R_E$:

$$\delta V_S(r, \theta, \phi) = \sum_{k=1}^{21} \sum_{l=0}^{20} \sum_{m=-l}^{l} v_{klm} Z_k(r) Y_{lm}(\theta, \phi), \tag{B9}$$

where $\Delta V_s$ is shear wave velocity anomaly relative to PREM, and $Z_r$ are the splines. Using the procedures of *Ritsema et al.* [2007], we project our input models onto this basis and then apply the S20RTS resolution filter to obtain the coefficients of the synthetic velocity anomaly, $s_{klm}$. We calculate the local correlation coefficient between the

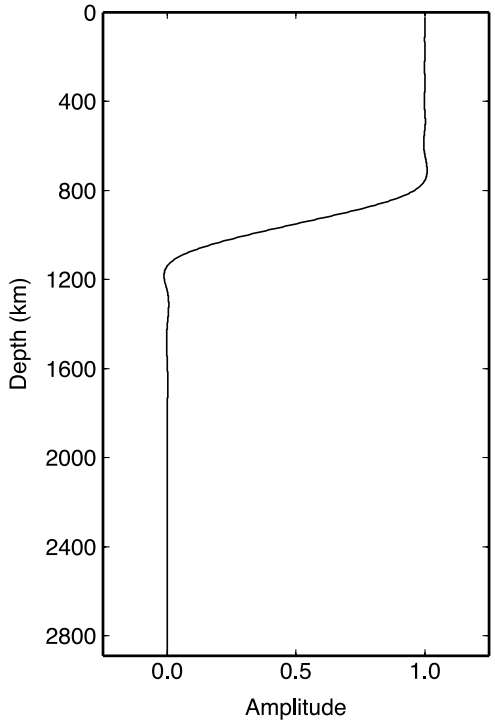


**Figure B1.** Profile of the function used to weight the correlation of model and observed tomography to the uppermost mantle. This weighting function emphasizes the correlation in the uppermost 800 km of the mantle, the region which contains the anomalous shear wave velocities observed beneath the Congo basin.

synthetic and S20RTS for each spline using [*Toksöz et al.*, 1969]

$$c_k(\Omega) = \frac{\sum_{l=0}^{20}\sum_{m=-l}^{l} v_{klm}(\Omega)s_{klm}(\Omega)}{\sqrt{\sum_{l=0}^{20}\sum_{m=-l}^{l} v_{klm}^2(\Omega)\sum_{l=0}^{20}\sum_{m=-l}^{l} s_{klm}^2(\Omega)}}, \tag{B10}$$

where $v_{klm}(\Omega)$ and $s_{klm}(\Omega)$ are the coefficients of S20RTS and the synthetic tomography, respectively, after being localized near the Congo basin. The coefficients $c_k$ provide a representation of the localized correlation as a function of depth:

$$c(r,\Omega) = \sum_{k=1}^{21} c_k(\Omega)Z_k(r). \tag{B11}$$

We calculate a weighted average of this correlation function using a weighting function, $g(r)$, whose support is the uppermost mantle (depth < 1000 km) and whose amplitude is constant throughout $r < 800$ km (Figure B1):

$$C = \frac{\int_{R_{CMB}}^{R_E} g(r)c(r,\Omega)dr}{\int_{R_{CMB}}^{R_E} g(r)dr} = \frac{\sum_{k=1}^{21} g_k c_k(\Omega)}{\sum_{k=1}^{21} g_k}, \tag{B12}$$

where $g_k$ are the coefficients of the filter $g$ in the spline basis. $C$ is a measure of the correlation between the synthetic tomography and S20RTS localized near the Congo and to a depth less than 1000 km.

[60] **Acknowledgments.** This is contribution 10019 of the Division of Geological and Planetary Sciences and 107 of the Tectonics Observatory, Caltech. All calculations carried out on the Caltech Geosciences Supercomputer Facility partially supported by NSF EAR-0521699. Additional support provided through the Tectonics Observatory by the Gordon and Betty Moore Foundation. Much of the analysis presented in this paper was carried out while N. J. D. was a visiting student in the Department of Earth and Planetary Sciences, Harvard University. We thank Dan Schrag, Rick O'Connell, and John Shaw for their generous support. We also thank Jeroen Ritsema for help with analysis of the tomographic data. We thank Nicky White and Mike Daly for their insightful reviews of this paper.

## References

Anderson, D. L. (2007a), The eclogite engine: Chemical geodynamics as a Galileo thermometer, in *Plates, Plumes and Planetary Processes*, edited by G. R. Foulger and D. M. Jurdy, *Spec. Pap. Geol. Soc. Am.*, *430*, 47–64, doi:10.1130/2007.2430(03).

Anderson, D. L. (2007b), *New Theory of the Earth*, Cambridge Univ. Press, Cambridge, U. K.

Ayele, A. (2002), Active compressional tectonics in central Africa and implications for plate tectonic models: Evidence from fault mechanism studies of the 1998 earthquakes in the Congo basin, *J. Afr. Earth Sci.*, *35*, 45–50, doi:10.1016/S0899-5362(02)00098-2.

Basri, R., and D. W. Jacobs (2003), Lambertian reflectance and linear subspaces, *IEEE Trans. Pattern Anal. Mach. Intell.*, *25*, 218–233, doi:10.1109/TPAMI.2003.1177153.

Billen, M. I., M. Gurnis, and M. Simons (2003), Multiscale dynamics of the Tonga-Kermadec subduction zone, *Geophys. J. Int.*, *153*, 359–388, doi:10.1046/j.1365-246X.2003.01915.x.

Burke, K. (1976), The Chad basin: An active intra-continental basin, *Tectonophysics*, *36*, 197–206, doi:10.1016/0040-1951(76)90016-0.

Cahen, L. (1954), *Géologie du Congo Belge*, H. Vaillant-Carmanne, Liège, France.

Cahen, L., J. J. Ferrand, M. J. F. Haarsma, L. Lepersonne, and T. Verbeek (1959), Description du sondage de Samba, *Ann. Mus. R. Congo Belge Sci. Geol.*, *29*.

Cahen, L., J. J. Ferrand, M. J. F. Haarsma, L. Lepersonne, and T. Verbeek (1960), Description du sondage de Dekese, *Ann. Mus. R. Congo Belge Sci. Geol.*, *34*.

Commission for the Geological Map of the World (1987), International geological map of Africa, scale 1:500,000, 6 panels, UNESCO, Paris, France.

Conrad, C. P., and P. Molnar (1999), Convective instability of a boundary layer with temperature- and strain-rate-dependent viscosity in terms of 'available buoyancy', *Geophys. J. Int.*, *139*, 51–68, doi:10.1046/j.1365-246X.1999.00896.x.

Daly, M. C., S. R. Lawrence, D. Kumin'a, and M. Binga (1991), Late Paleozoic deformation in Africa: A result of distant collision?, *Nature*, *350*, 605–607, doi:10.1038/350605a0.

Daly, M. C., S. R. Lawrence, K. Diemu-Tshiband, and B. Matouana (1992), Tectonic evolution of the Cuvette Centrale, Zaire, *J. Geol. Soc.*, *149*, 539–546, doi:10.1144/gsjgs.149.4.0539.

DeRito, R. F., F. A. Cozzarelli, and D. S. Hodge (1983), Mechanism of subsidence of ancient cratonic rift basins, *Tectonophysics*, *94*, 141–168, doi:10.1016/0040-1951(83)90014-8.

De Waele, B., S. P. Johnson, and S. A. Pisarevsky (2008), Paleoproterozoic to Neoproterozoic growth and evolution of the eastern Congo Craton: Its role in the Rodinia puzzle, *Precambrian Res.*, *160*, 127–141, doi:10.1016/j.precamres.2007.04.020.

Dziewonski, A. M., and D. L. Anderson (1981), Preliminary reference Earth model, *Phys. Earth Planet. Inter.*, *25*, 297–356, doi:10.1016/0031-9201(81)90046-7.

Évrard, P. (1957), Les recherches géophysiques at géologiques et le travaux de sondage dans la Cuvette congolaise, *Mem. Acad. R. Sci. Colonials Classe Sci. Tech.*, *VII*, 1.

Farr, T. G., et al. (2007), The Shuttle Radar Topography Mission, *Rev. Geophys.*, *45*, RG2004, doi:10.1029/2005RG000183.

Giresse, P. (2005), Mesozoic-Cenozoic history of the Congo basin, *J. Afr. Earth Sci.*, *43*, 301–315, doi:10.1016/j.jafrearsci.2005.07.009.

Grand, S. P. (2002), Mantle shear-wave tomography and the fate of subducted slabs, *Philos. Trans. R. Soc. London, Ser. A*, *360*, 2475–2491, doi:10.1098/rsta.2002.1077.

Gu, Y. J., A. M. Dziewonski, W. Su, and G. Ekström (2001), Models of the mantle shear velocity and discontinuities in the pattern of lateral heterogeneities, *J. Geophys. Res.*, *106*, 11,169–11,199, doi:10.1029/2001JB000340.

Hanne, D., N. White, A. Butler, and S. Jones (2004), Phanerozoic vertical motions of Hudson Bay, *Can. J. Earth Sci.*, *41*, 1181–1200, doi:10.1139/e04-047.

Hartley, R. W., and P. A. Allen (1994), Interior cratonic basins of Africa: Relation to continental break-up and role of mantle convection, *Basin Res.*, *6*, 95–113, doi:10.1111/j.1365-2117.1994.tb00078.x.

Hartley, R. W., A. B. Watts, and J. D. Fairhead (1996), Isostasy of Africa, *Earth Planet. Sci. Lett.*, *137*, 1–18, doi:10.1016/0012-821X(95)00185-F.

Ingersoll, R. V., and C. J. Busby (1995), Tectonics of sedimentary basins, in *Tectonics of Sedimentary Basins*, edited by C. J. Busby and R. V. Ingersoll, pp. 1–51, Blackwell, Boston, Mass.

Jordan, T. H. (1978), Composition and development of the continental tectosphere, *Nature*, *274*, 544–548, doi:10.1038/274544a0.

Karato, S. (2008), *Deformation of Earth Materials: An Introduction to the Rheology of Solid Earth*, Cambridge Univ. Press, Cambridge, U. K.

Kaus, B. J. P., J. A. D. Connolly, Y. Y. Podladchikov, and S. M. Schmalholz (2005), Effect of mineral phase transitions on sedimentary basin subsidence and uplift, *Earth Planet. Sci. Lett.*, *233*, 213–228, doi:10.1016/j.epsl.2005.01.032.

Kelly, R. K., P. B. Kelemen, and M. Jull (2003), Buoyancy of the continental upper mantle, *Geochem. Geophys. Geosyst.*, *4*(2), 1017, doi:10.1029/2002GC000399.

McGovern, P. J., S. C. Solomon, D. E. Smith, M. T. Zuber, M. Simons, M. A. Wieczorek, R. J. Phillips, G. A. Neumann, O. Aharonson, and J. W. Head (2002), Localized gravity/topography admittance and correlation spectra on Mars: Implications for regional and global evolution, *J. Geophys. Res.*, *107*(E12), 5136, doi:10.1029/2002JE001854.

McKenzie, D. (2003), Estimating $T_e$ in the presence of internal loads, *J. Geophys. Res.*, *108*(B9), 2438, doi:10.1029/2002JB001766.

McKenzie, D., and D. Fairhead (1997), Estimates of the effective elastic thickness of the continental lithosphere from Bouguer and free air gravity anomalies, *J. Geophys. Res.*, *102*, 27,523–27,552, doi:10.1029/97JB02481.

McNutt, M. (1979), Compensation of oceanic topography: An application of the response function technique to the *Surveyor* area, *J. Geophys. Res.*, *84*, 7589–7598.

Mégnin, C., and B. Romanowicz (2000), The three-dimensional shear velocity structure of the mantle from the inversion of body, surface and higher-mode waveforms, *Geophys. J. Int.*, *143*, 709–728, doi:10.1046/j.1365-246X.2000.00298.x.

Middleton, M. F. (1989), A model for the formation of intracratonic sag basins, *Geophys. J. Int.*, *99*, 665–676, doi:10.1111/j.1365-246X.1989.tb02049.x.

Naimark, B. M., and A. T. Ismail-Zadeh (1995), Numerical models of a subsidence mechanism in intracratonic basins: Application to North American basins, *Geophys. J. Int.*, *123*, 149–160, doi:10.1111/j.1365-246X.1995.tb06667.x.

O'Connell, R. J., and G. J. Wasserburg (1972), Dynamics of submergence and uplift of a sedimentary basin underlain by a phase-change boundary, *Rev. Geophys. Space Phys.*, *10*, 335–368, doi:10.1029/RG010i001p00335.

Pasyanos, M. E., and A. A. Nyblade (2007), A top to bottom lithospheric study of Africa and Arabia, *Tectonophysics*, *444*, 27–44, doi:10.1016/j.tecto.2007.07.008.

Pavlis, N. K., and R. H. Rapp (1990), The development of an isostatic gravitational model to degree 360 and its use in global gravity modeling, *Geophys. J. Int.*, *100*, 369–378.

Priestly, K., and D. McKenzie (2006), The thermal structure of the lithosphere from shear wave velocities, *Earth Planet. Sci. Lett.*, *244*, 285–301, doi:10.1016/j.epsl.2006.01.008.

Ritsema, J., and H. J. van Heijst (2000), New seismic model of the upper mantle beneath Africa, *Geology*, *28*, 63–66, doi:10.1130/0091-7613(2000)28<63:NSMOTU>2.0.CO;2.

Ritsema, J., and H. J. van Heijst (2004), Global transition zone tomography, *J. Geophys. Res.*, *109*, B02302, doi:10.1029/2003JB002610.

Ritsema, J., H. J. van Heijst, and J. H. Woodhouse (1999), Complex shear wave velocity anomaly structure imaged beneath Africa and Iceland, *Science*, *286*, 1925–1928, doi:10.1126/science.286.5446.1925.

Ritsema, J., A. K. McNamara, and A. L. Bull (2007), Tomographic filtering of geodynamic models: Implications for model interpretation and large-scale mantle structure, *J. Geophys. Res.*, *112*, B01303, doi:10.1029/2006JB004566.

Sahagian, D. L. (1993), Structural evolution of African basins: Stratigraphic synthesis, *Basin Res.*, *5*, 41–54, doi:10.1111/j.1365-2117.1993.tb00055.x.

Simons, M. (1996), Localization of gravity and topography: Constraints on the tectonics and mantle dynamics of Earth and Venus, Ph.D. thesis, Mass. Inst. of Technol., Cambridge.

Simons, M., S. Solomon, and B. H. Hager (1997), Localization of gravity and topography: Constraints on the tectonics and mantle dynamics of Venus, *Geophys. J. Int.*, *131*, 24–44, doi:10.1111/j.1365-246X.1997.tb00593.x.

Sleep, N. H. (2005), Evolution of the continental lithosphere, *Annu. Rev. Earth Planet. Sci.*, *33*, 369–393, doi:10.1146/annurev.earth.33.092203.122643.

Sloss, L. L. (1988), Tectonic evolution of the craton in Phanerozoic time, in *The Geology of North America*, vol. D2, *Sedimentary Cover of the North American Craton: U.S.*, edited by L. L. Sloss, pp. 25–51, Geol. Soc. of Am., Boulder, Colo.

Sloss, L. L. (1990), Epilog, in *Interior Cratonic Basins*, edited by M. W. Leighton et al., *AAPG Mem.*, *51*, 729–797.

Tamisiea, M. E., J. X. Mitrovica, and J. L. Davis (2007), GRACE gravity and data constrain ancient ice geometries and continental dynamics over Laurentia, *Science*, *316*, 881–883, doi:10.1126/science.1137157.

Tan, E., and M. Gurnis (2007), Compressible thermochemical convection and application to lower mantle structures, *J. Geophys. Res.*, *112*, B06304, doi:10.1029/2006JB004505.

Tapley, B., et al. (2005), GGM02—An improved Earth gravity field model from GRACE, *J. Geod.*, *79*, 467–478, doi:10.1007/s00190-005-0480-z.

Toksöz, M. N., J. Arkani-Hamed, and C. A. Knight (1969), Geophysical data and long-wave heterogeneities of the Earth's mantle, *J. Geophys. Res.*, *74*, 3751–3770.

Turcotte, D. L., R. J. Willemann, W. F. Haxby, and J. Norberry (1981), Role of membrane stresses in support of planetary topography, *J. Geophys. Res.*, *86*, 3951–3959, doi:10.1029/JB086iB05p03951.

Varshalovich, D. A., A. N. Moskalev, and V. R. Kjersonskii (1988), *Quantum Theory of Angular Momentum*, World Sci., Singapore.

Watts, A. B., and W. B. F. Ryan (1976), Flexure of the lithosphere and continental margin basins, *Tectonophysics*, *36*, 25–44, doi:10.1016/0040-1951(76)90004-4.

Wieczorek, M. A. (2007), The gravity and topography of the terrestrial planets, in *Treatise on Geophysics*, vol. 10, *Planets and Moons*, edited by T. Spohn, pp. 165–206, doi:10.1016/B978-044452748-6.00156-5, Elsevier, New York.

Zhong, S. J., M. Gurnis, and G. Hulbert (1993), Accurate determination of surface normal stress in viscous flow from a consistent boundary flux method, *Phys. Earth Planet. Inter.*, *78*, 1–8.

N. J. Downey, Institute for Geophysics, University of Texas at Austin, J. J. Pickle Research Campus Building 196, 10100 Burnet Road (R2200), Austin, TX 78758-4445, USA. (ndowney@ig.utexas.edu)

M. Gurnis, Seismological Laboratory 252-21, California Institute of Technology, 1200 East California Boulevard, Pasadena, CA 91125, USA.